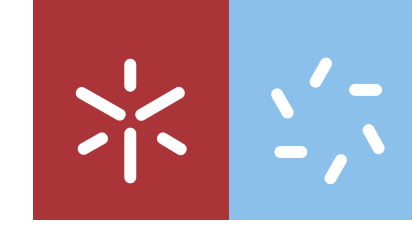**Universidade do Minho**
Escola de Ciências

Yue Li

High performance cobalt-based phosphide catalysts for electrochemical water splitting

High performance cobalt-based phosphide catalysts for electrochemical water splitting

Yue Li

UMinho | 2019

outubro de 2019

Yue Li

High performance cobalt-based phosphide catalysts for electrochemical water splitting
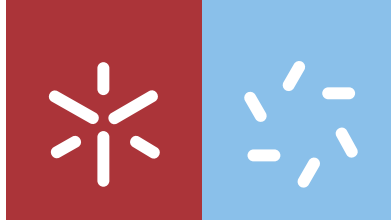
DECLARATION

Name: Yue Li

E-mail address: pg33717@uminho.pt

Phone: +351 934953083

Identity Card Number: E24973859

Title of dissertation: High performance cobalt-based phosphide catalysts for electrochemical water splitting

Supervisors:

Professora Doutora Isabel Correia Neves, Department of Chemistry, School of Sciences, University of Minho;

Doutor Lifeng Liu, Nanomaterials for Energy Storage and Conversion (NESC) Group, Department of Quantum and Energy Materials, Energy Materials Unit, International Iberian Nanotechnology Laboratory (INL)

Year of completion: 2019

Master in Chemical Analysis and Characterization Techniques

IN ACCORD TO LEGISLATION IN VIGOR, THE REPRODUCTION OF ANY PART OF THIS THESIS IS NOT ALLOWED.

University of Minho, _____/_____/_____

Signature:

Acknowledgments

Abstract

Hydrogen has been proposed to be a clean and carbon-neutral energy carrier that can be used as next-generation fuel. Water splitting has long been thought to be a sustainable and environmentally friendly approach to hydrogen production, given that water is virtually an inexpensive, renewable, plenty resource and water splitting process itself does not produce any harmful emissions. The major challenge for the development of water electrolyzers for large scale production of hydrogen is huge energy consumption, originating from high overpotentials of the oxygen evolution reaction (OER) and the hydrogen evolution reaction (HER). Transition metal phosphides have recently emerged as a new class of electrocatalysts that can efficiently catalyze the OER and HER. However, the catalytic performance needs to be further improved to promote the practical application of phosphide catalysts in the water splitting . In this work, two strategies are investigated to increase the hydrogen evolution reaction, oxygen evolution reaction as well as the overall water splitting performance of phosphide catalysts.

The first strategy is to dope nickel atoms into cobalt-based phosphide catalysts to improve the intrinsic activity of each active site. The as-synthesized powdery phosphide catalysts showed narrow particle size distribution of 5-10 nm and good water splitting performance. Low overpotentials of 0.26 and 0.13 V could deliver a benchmark current density of 10 mA cm^{-2} in 1.0 M KOH for the oxygen and hydrogen evolution, respectively. Benefitting from the excellent OER and HER catalytic performance, a low cell voltage of 1.70 V was needed for the overall water splitting at 10 mA cm^{-2}, outperforming the performance of noble metal based catalysts under the same conditions. Meanwhile, the electrolyzer was able to operate at 10 mA cm^{-2} over 40 h with negligible degradation, showing good long-term stability. The second strategy is to prepare self-supported porous cobalt phosphide to increase the number of active sites on a given geometric surface area of electrodes. The as-prepared porous cobalt phosphide self-supported electrode showed outstanding water splitting performance, especially at high current densities. For instance, to afford overall water splitting at an industry-relevant current density of 1000 mA cm^{-2}, a low voltage of only 1.98 V was required. More importantly, the electrolyzer could sustain continuous electrolysis for 500 h at 500 mA cm^{-2} without obvious degradation.

Key words: Water splitting, Electrocatalysis, Transition metal phosphide catalyst, Hydrogen evolution reaction, Oxygen evolution reaction

Resumo

O hidrogênio foi proposto como um transportador de energia limpo e neutro em carbono que pode ser usado como combustível da próxima geração. Há muito que se pensa que a eletrólise da água é uma abordagem sustentável e ecológica da produção de hidrogênio, uma vez que a água é praticamente um recurso barato, renovável e com muitos recursos, e o próprio processo de separação de água não produz emissões nocivas. O grande desafio para o desenvolvimento de eletrocatalisadores de água para produção em larga escala de hidrogênio é o enorme consumo de energia, originado de altos superpotenciais da reação de evolução de oxigênio (OER) e da reação de evolução de hidrogênio (HER). Os fosfitos metálicos de transição surgiram recentemente como uma nova classe de eletrocatalisadores que podem catalisar eficientemente o OER e o HER. No entanto, o desempenho catalítico precisa ser melhorado para promover a aplicação prática de catalisadores de fosfito na eletrólise da água. Neste trabalho, duas estratégias foram investigadas para aumentar o desempenho da separação de água de catalisadores de fosfito.

A primeira estratégia é dopar átomos de níquel em catalisadores de fosfito de cobalto para melhorar a atividade intrínseca de cada sítio ativo. Os catalisadores de fosfito em pó como sintetizados mostraram uma distribuição estreita do tamanho de partícula de 5 a 10 nm e bom desempenho de separação de água. Superpotenciais baixos de 0,26 e 0,13 V podem fornecer uma densidade de corrente de referência de 10 mA cm^{-2} em KOH 1,0 M para a evolução de oxigênio e hidrogênio, respectivamente. Foi necessária uma voltagem de célula baixa de 1,70 V para a divisão geral da água a 10 mA cm^{-2}, comparável ao desempenho de catalisadores à base de metais nobres. Enquanto isso, o eletrolisador foi capaz de operar a 10 mA cm^{-2} por 40 h com degradação desprezível. A segunda estratégia foi preparar fosfito de cobalto poroso auto-suportado para aumentar o número de locais ativos em uma determinada área geométrica da superfície dos elétrodos. O elétrodo poroso autoportante preparado mostrou excelente desempenho de separação de água, especialmente em altas densidades de corrente. Por exemplo, para permitir a divisão geral da água a uma densidade de corrente relevante para o setor de 1000 mA cm^{-2}, foi necessário uma baixa tensão de 1,98 V. Mais importante, o eletrolisador poderia sustentar eletrólise contínua por 500 h a 500 mA cm^{-2} sem degradação óbvia.

Palavras-chave: Separação de água, Eletrocatálise, Catalisador de fosfito metálico de transição, reação de evolução de hidrogênio, reação de evolução de oxigênio

Table of Contents

List of Abbreviations and Acronyms

CP	Carbon paper
CF	Cobalt foam
CV	Cyclic Voltammetry
DI water	Deionized water
EG	Ethylene glycol
GC	Glycerol
GE	Galvanostatic electrolysis
HRTEM	High resolution Transmission Electron Microscopy
HER	Hydrogen evolution reaction
HADDF	High-angle annular dark-field
ICDD	International Centre for Diffraction Data
NP	Nanoparticle
OWE	Overall water splitting
OER	Oxygen evolution reaction
PEM	Proton exchange membrane
RHE	Reversible hydrogen electrode
SCE	Saturated calomel electrode
SEM	Scanning Electron Microscopy
STEM	Scanning transmission electron microscopy
TMP	Transition metal phosphide
TEM	Transmission Electron Microscopy
TOP	Trioctylphosphine
XRD	X-ray Diffraction
XPS	X-ray Photoelectron Spectroscopy
η	Overpotential
b	Tafel slope

List of Figures

List of Tables

Chapter 1. Introduction

This chapter aims to provide an overview about the current state of the world's energy demand, the status of development, bottleneck and latest findings of hydrogen energy in the context of water splitting . It also describes present understanding of water splitting mechanism and a general overview of catalyst development.

1.1 World energy and environment status

The huge increase in the world population as well as the changes in the lifestyle and standards of living, substantially boosts the global energy demand and thus the demanding for the associated resources (Acar & Dincer, 2014). The global economy grew by 3.7% in 2018, higher than the average annual growth rate since 2010. Such rapid economic development has also driven higher energy demand. According to the Global Energy & CO_2 Status Report 2018 (International Energy Agency, 2019), the total energy demand of 2018 worldwide grew nearly twice than that since 2010, due to the strong global economy development and increased heating and cooling demand in some parts of the world. Natural gas has become the first choice of the fuel in 2018, accounting for nearly 45% of total consumable energy. Demand for all fuels has increased, which makes consumption of fossil fuels grow by nearly 70% for the second consecutive year.

Nowadays, as shown in Figure 1, fossil fuels (e.g. coal, oil, natural gas) are still the dominant sources of global energy demand, resulting in almost 100% of CO_2 emissions in the world.
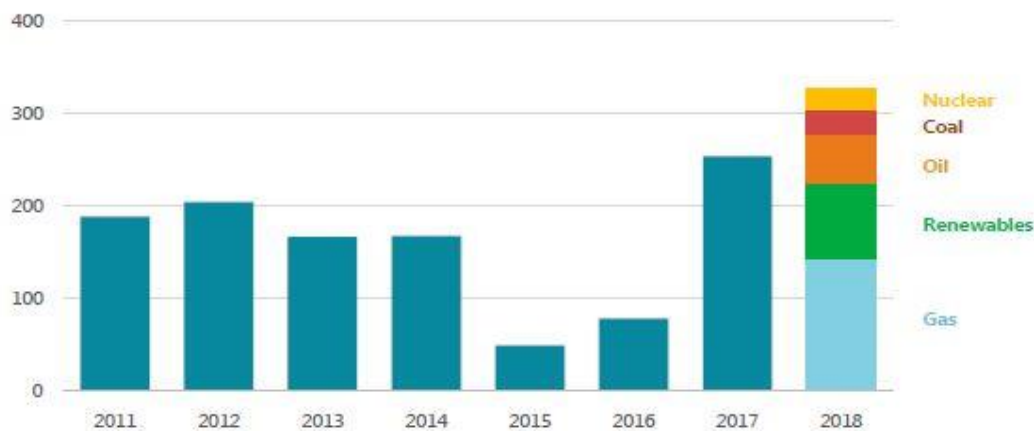
Figure 1. Average annual global primary energy demand growth by fuel, 2010-2018 (International Energy Agency, 2019)

As a result, the global CO_2 emissions increased by 1.7% in 2018, due to higher energy demand (Figure 2). At current consumption rates, world's proven coal, oil and natural gas reserves are expected to last for approximately 200, 40 and 60 years, respectively. Afterwards, the overall resources will decline (Baykara, 2018). The depletion of fossil resources and the associated environmental pollution are the common themes of today's global concern.
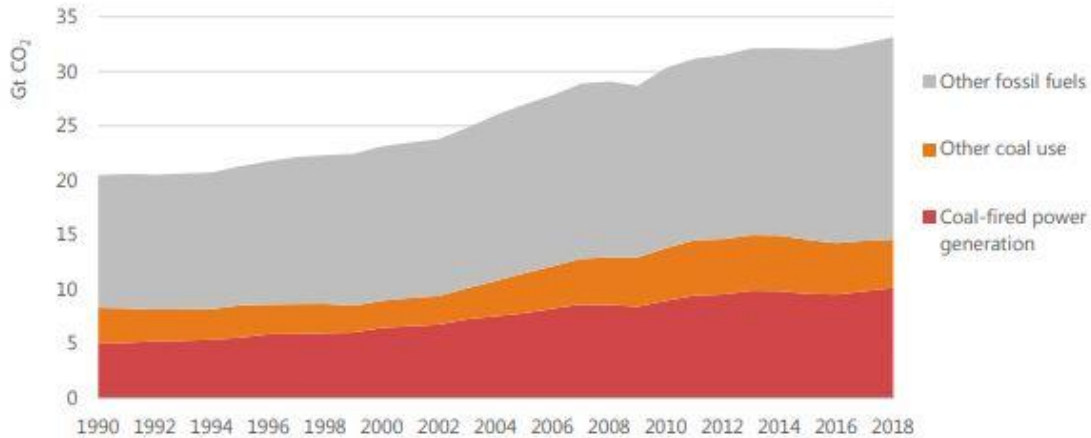
Figure 2. Global energy-related carbon dioxide emissions by source, 1990-2018 (International Energy Agency, 2019)

At the same time, the growing trend of world energy demand is expected to continue in the future. Generally speaking, the global energy system faces two challenges of 'more energy and less carbon'. As a result, it is necessary to increase the energy production capability. Seeking for safer, cleaner and more diverse energy sources may be a feasible strategy to reduce or/and eliminate greenhouse gas emissions and meanwhile meet world energy demand. Thus, a renewable clean alternative is the prime requisite now (Evans, Strezov, & Evans, 2009). The use of renewable resources could minimize environmental impacts, produce minimum secondary wastes, and are sustainable based on current and future economic and social societal needs. These resources are easy to replenish and never exhausted (Mignon & Bergek, 2016). Renewable energy has only grown in just a few decades, and many countries are investing heavily to capitalize on these resources (Taljan & Gubina, 2009).

1.2 Hydrogen

Among all renewable energy sources, hydrogen is a globally recognized secondary form of renewable energy and is a promising substitute for fossil fuels (Nikolaidis & Poullikkas, 2017). Hydrogen is the simplest element in the periodic table of elements, but hydrogen has the highest energy density per unit mass of all fuels (Baykara, 2018). It is also the most abundant element in the universe, accounting for about 75% of all matter. It is the tenth richest element in the earth's crust. Despite it is richness and simplicity, hydrogen cannot be produced naturally like the gas on Earth, since combining hydrogen with other elements is an uphill reaction and cannot be happen spontaneously.

1.2.1 Advantages of hydrogen

Further advantages of hydrogen as a promising alternative to fossil fuels are as follows (Kaur & Pal, 2019):

1. It is widely distributed in nature in the form of a compound, particularly H_2O, which is the most abundant compound on the planet;

2. Hydrogen is environmentally friendly since consumption of hydrogen does not leave any harmful substances or waste. Moreover, when used in fuel cells, the produced water as a by-product can be further utilized to produce more hydrogen;

3. Hydrogen has an inexpensive maintenance cost, although the initial installation price can be high;

4. The most important aspect of hydrogen energy is its reproducibility and ease of synthesis of large amounts of hydrogen molecules.

1.2.2 Applications of hydrogen

Hydrogen is widely used in different ways as mentioned below:

1. Hydrogen fuel cell - These fuel cells generate energy from oxygen and hydrogen leaving water as a clean by-product, which could be used as a fuel source in submarines, cars, space crafts, etc., (Belz, 2016);

2. The source of fuel in vehicles - It is replacing fossil fuels such as coal, natural gas and diesel in cars, ships, submarines and even rockets (Staffell *et al.*, 2019);

3. Power Generation – Hydrogen is used as a fuel in various power plants to generate electricity (Lewis & Nocera, 2006);

4. Applications in industry and other fields - In the food industry, it is used in the manufacture of hydrogenated vegetable oils (Pinto *et al.*, 2014). The petrochemical industry also uses hydrogen to refine crude oil (Elreedy & Tawfik, 2015); it is used in the chemical industry to extract hydrogen from metals (Eatwell-Hall, Sharifi, & Swithenbank, 2010) and to synthesize compounds (Heng, Zhang, & Xiao, 2016).

1.2.3 Hydrogen production

Nowadays, there are several techniques to generate hydrogen. Depending on the used raw materials, the processes used for hydrogen production can be divided into two broad categories, namely conventional technology and renewable technology. Figure 3 shows the various pathways for hydrogen production (Nikolaidis & Poullikkas, 2017).

In the first type of process, hydrogen is primarily derived from fossil fuels, including processes for hydrocarbon reforming and pyrolysis. In the hydrocarbon reforming process, it is mainly composed of steam reforming, partial oxidation and autothermal steam reforming. The second type of process is to produce hydrogen from renewable resources, either biomass or water. Using biomass as a feedstock, these methods can be subdivided into two general sub-categories, thermochemical and biological processes. The second type of renewable technology involves producing hydrogen by water splitting processes such as electrolysis, thermolysis and photolysis.
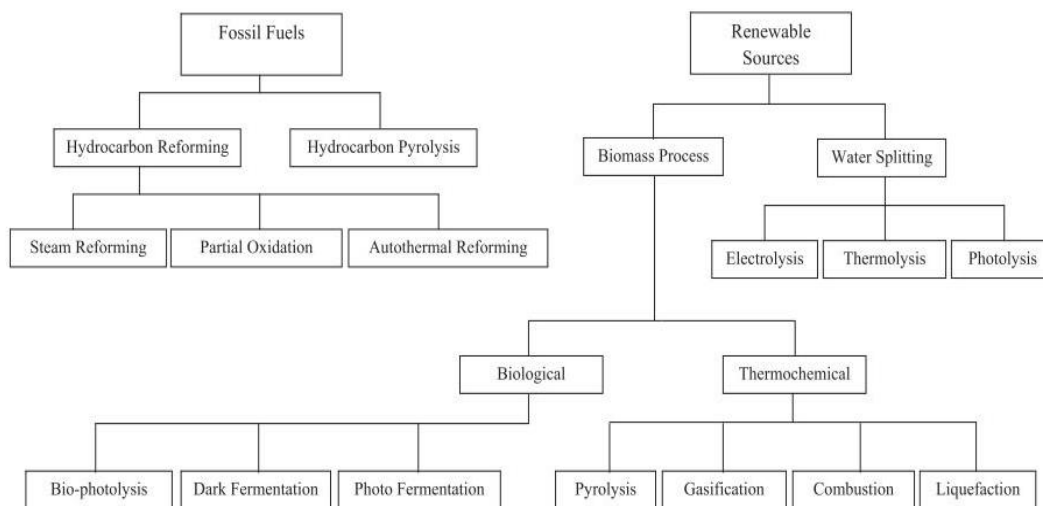
Figure 3. Hydrogen production methods (Nikolaidis & Poullikkas, 2017).

Photoelectrochemical and electrochemical water splitting are two promising strategies for achieving hydrogen production from renewable sources. However, due to the limitation of operating current densities, photoelectrochemical water splitting devices require much larger electrode areas than electrochemical water splitting systems to produce the same amount of gas per unit time, resulting in restrictions in choosing viable catalysts and suitable construction locations. In addition, other renewable energy sources are naturally

excluded from the photoelectrochemical pathway. Therefore, electrochemical water splitting is more attractive due to its greater flexibility and applicability. This hydrogen production process does not release carbon dioxide and requires only water and "green" electricity. Further, electrochemical water splitting produces high purity hydrogen, which can be directly used as an industrial raw material or a fuel gas for domestic use (Zhao, Rui, Dou, & Sun, 2018).

1.3 Water splitting

1.3.1 History of the water splitting

The history of water splitting dates back to the 1st industrial revolution. In 1800, William Nicolson and Anthony Carlise used the voltaic pile for water splitting. It was confirmed for the first time that the gases produced by water splitting were hydrogen and oxygen, and their potential applications were gradually confirmed (Hofmannz, 1998). After the mid-19th century, with the development of industry, water splitting became an inexpensive method of hydrogen production. In the 1920s and 1930s various water splitting designs were developed, and several large 100 MW power plants were built around the world during the same period (LeRoy, 1983). However, the development of water splitting, which was stopped during the Second World War, was not able to continue until the oil crisis of the 1970s, as the hydrogen from water splitting was proposed to be a promising way to solve the energy crisis and sustainable supply problems (J. O'M. Bockris, Conway, Yeager, & White, 1981).

1.3.2 Electrolyzers used for water splitting

According to the electrolyte, ionic agent (OH^-, H^+, O_2) and operating temperature, water electrolyzers are divided into three categories: alkaline, proton exchange membrane (PEM) and solid oxide electrolyzers. Each type of electrolyzer has its own advantages and disadvantages, but these three technologies are attractive and promising for sustainable energy applications. Up to now, alkaline electrolyzers has become the most commonly used and studied technology (Zeng & Zhang, 2010) (Figure 4).
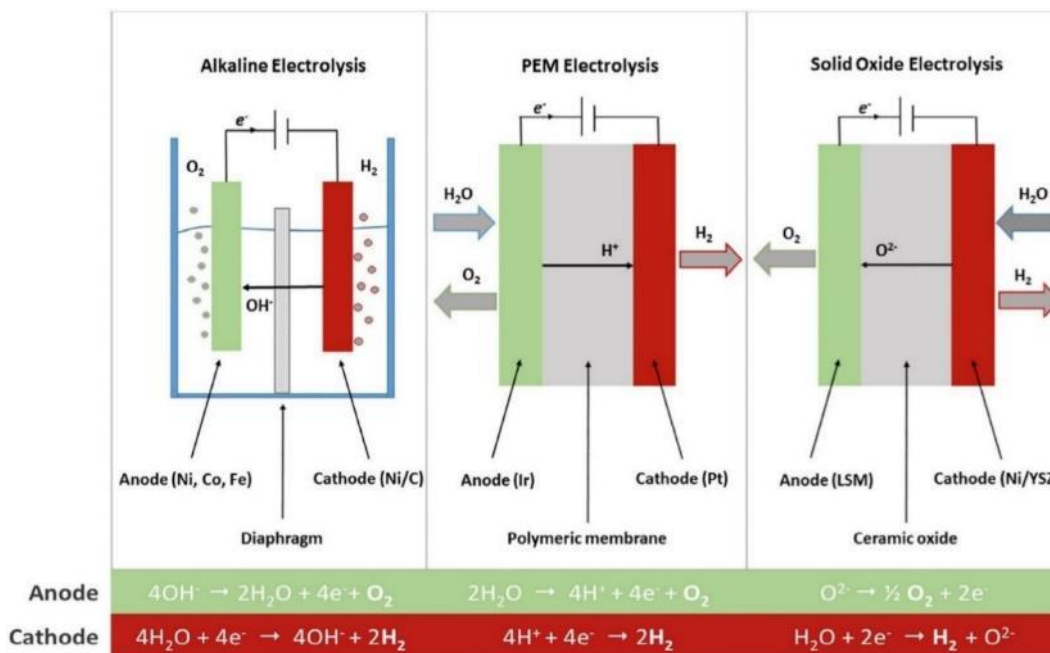
Figure 4. Operation principles of alkaline, PEM and solid oxide water electrolyzers (Zeng & Zhang, 2010).

1.3.3 Chemical reactions of water splitting

In a typical water splitting system (Figure 5, using PEM water electrolyzer as example), H_2 and O_2 are produced at the cathode and the anode, respectively, through the hydrogen evolution reaction (HER) and the oxygen evolution reaction (OER), as described in Equation (1.1) and (1.2), respectively (Zhao *et al.*, 2018).

$$\text{HER: } 4e^- + 4H^+(aq) \longrightarrow 2H_2(g) \tag{1.1}$$

$$\text{OER: } 2H_2O(l) \longrightarrow 4H^+(aq) + 4O_2(g) \tag{1.2}$$
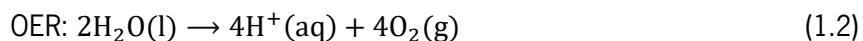
Under standard conditions, a thermodynamic voltage of 1.23 V is required to drive electrochemical water splitting, which corresponds to an energy input of Gibbs free energy of 237.1 kJ mol^{-1}. However, the slow dynamics of HER and OER require high overpotentials to achieve appreciable current density, resulting in relatively low energy conversion efficiencies. Therefore, the input voltage of water splitting in the practical electrolyzers is much larger than 1.23V (You & Sun, 2018).
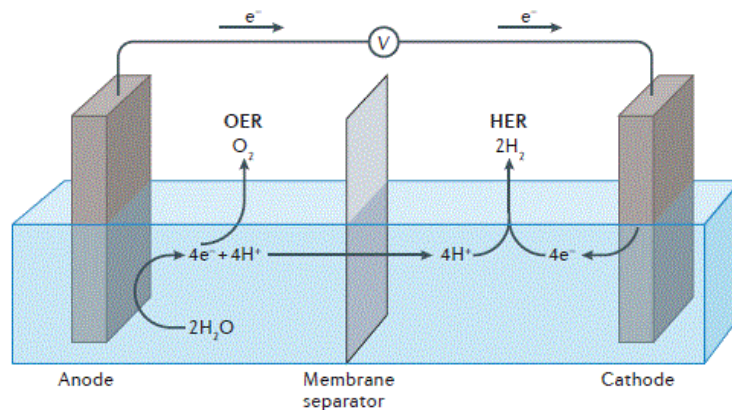
Figure 5. Schematic of water electrolyzers (Zhao *et al.*, 2018).

1.3.4 Mechanism of the HER

The HER (Equation (1.1)) is a two-electron transfer process taking place at the electrode/electrolyte, which occurs via two individual steps through either the Volmer–Heyrovsky or the Volmer–Tafel mechanism, as shown in Figure 6 (Morales-Guio, Stern, & Hu, 2014).
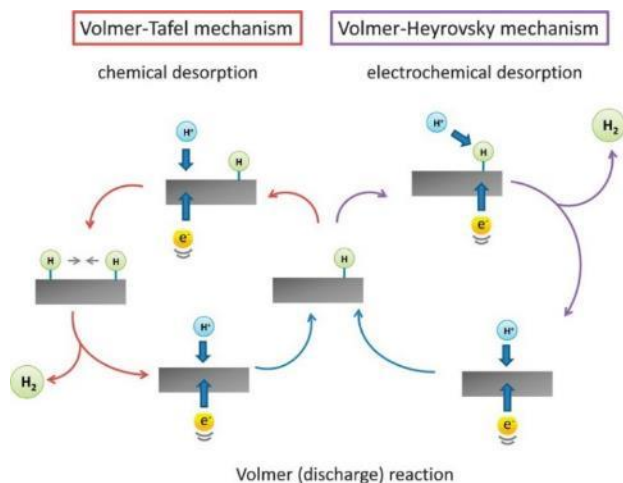
Figure 6. The mechanism of HER on the surface of an electrode in acidic solution (Morales-Guio *et al.*, 2014).

It has generally been accepted that the HER comprises two successive steps. In the beginning, an electron-coupled H^+ transfers to the electrode to yield an absorbed hydrogen atom (H^*). After this step, two possible pathways may proceed for H_2 evolution. If the surface coverage of H^* is low, the single H^* atom would preferably join with a proton and an electron simultaneously to form a molecule, which is named as the Heyrovsky step or the electrochemical desorption step. Alternatively, in the case of high surface coverage of

H*, two H* will recombine with each other on the electrode surface to form molecular H_2, which is recognized as the Tafel step or the chemical desorption step. Determining which pathway(s) is the rate-limiting step(s) can be simply done by Tafel analysis according to polarization curves.

In alkaline conditions, the HER is sluggish compared to that in acidic conditions because of water dissociation occurring prior to the formation of H* (Zhao *et al.*, 2018; Y. Wang, Kong, Zhao, Wang, & Selomulya, 2017; Joo, Kim, Lee, Choi, & Lee, 2019). The overall reactions and two-step processes of HER in acidic and alkaline solutions are shown in Table 1 (Jiao, Zheng, Jaroniec, & Qiao, 2015):

Table 1. The overall reactions and two-step processes of HER in acidic and alkaline solutions (Jiao *et al.*, 2015)

Acidic solution:	
Overall reaction:	$2H^+ + 2e^- \longrightarrow H_2$
1st step:	$H^+ + e^- + * \longrightarrow H^*$ (Volmer)
2nd step:	$H^+ + e^- + H^* \longrightarrow H_2$ (Heyrovsky) or $2H^* \longrightarrow H_2$ (Tafel)
Alkaline solution:	
Overall reaction:	$2H_2O + 2e^- \longrightarrow H_2 + 2OH^-$
1st step:	$H_2O + e^- \longrightarrow H^* + OH^-$ (Volmer)
2nd step:	$H_2O + e^- + H^* \longrightarrow H_2 + OH^-$ (Heyrovsky) or $2H^* \longrightarrow H_2$ (Tafel)

1.3.5 Mechanism of the OER

The OER is a four electron–proton coupled reaction taking place at the anode. Compared to HER, OER process is more sluggish in kinetics, involving three surface-absorbed intermediates: OOH*, O* and OH*.

Figure 7 shows the circular flow of the possible pathways in both acid and alkaline (Suen *et al.*, 2017). Generally, the mechanism of OER is believed to proceed by the first step of H_2O dissociation in acidic electrolytes or OH- coordination in alkaline electrolytes. Several possible mechanisms for OER have been proposed, and there are differences and similarities between them.
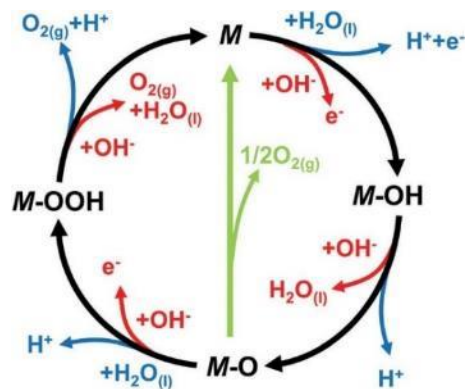
Figure 7. The OER mechanism for acid (blue line) and alkaline (red line) conditions (Suen *et al.*, 2017).

Most of the proposed mechanisms include the same intermediates, while the major difference lies in the formation of oxygen. There are two different approaches to forming an oxygen molecule from an O* intermediate. One is the direct combination of two O* (Figure 7, green route), and the other is the formation of the OOH* intermediate, which subsequently decomposes to O_2 (Figure 7, black route). Despite this difference, the consensus is that the electrocatalysis of OER is a heterogeneous reaction in which the M-O bonding interaction in the intermediate (OOH*, O* and OH*) is critical to the overall electrocatalytic ability. The overall reactions and four-step processes of OER in acidic and alkaline solutions are shown in Table 2 (Jiao *et al.*, 2015):

Table 2. The overall reactions and two-step processes of OER in acidic and alkaline solutions (Jiao *et al.*, 2015).

Acidic solution:	
Overall reaction:	$2H_2O \rightarrow O_2 + 4H^+ + 4e^-$
Reaction pathway:	$* + H_2O \rightarrow *OH + H^+ + e^-$
	$*OH \rightarrow *O + H^+ + e^-$
	$*O + H_2O \rightarrow OOH* + H^+ + e^-$
	$*OOH \rightarrow *O_2 + H^+ + e^-$
	$*O_2 \rightarrow * + O_2$
Alkaline solution:	
Overall reaction:	$4OH^- \rightarrow O_2 + 2H_2O + 4e^-$

Reaction pathway:	$* + OH^- \rightarrow *OH + e^-$
	$*OH + OH^- \rightarrow H_2O + *O + e^-$
	$*O + OH^- \rightarrow *OOH + e^-$
	$*OOH + OH^- \rightarrow *O_2 + e^-$
	$*O_2 \rightarrow * + O_2$

1.4 Electrocatalysts

Although electrochemical water splitting provides an effective method to produce high purity hydrogen, the practical application of electrochemical water splitting for large-scale hydrogen production is limited because it is a strong uphill reaction with a large overpotential. Development of electrocatalysts for OER and HER is an efficient way to overcome the large water splitting overpotentials (Walter *et al.*, 2010). The ideal catalyst for both HER and OER, must meet two basic requirements. First, the catalyst must be highly reactive and can produce a large current density with a minimum overpotential. Second, it must exhibit long-term stability. In addition, precious noble metals should be avoided to use considering the scalability of water electrolyzers.

1.4.1 Performance parameters for electrocatalysts

There are many electrocatalytic kinetic parameters to fairly evaluate the performance of electrocatalysts. These parameters are crucial and can offer insightful information with regards to the mechanism of the electrochemical reaction, which are described briefly in the following subsections.

1.4.1.1 Overpotential (η)

Overpotential is the difference between the experimentally observed potential and the thermodynamically determined potential of an electrochemical reaction, which is one of the most commonly used parameter to evaluate the performance of electrocatalysts. In ideal conditions, the applied potential for driving a specific reaction should be equal to the equilibrium potential. In actual situations, it always happens that the applied potential is higher than that at equilibrium in order to overcome the reaction kinetic barrier. According to the Nernst equation, the applied potential can be expressed in the equation (1.3),

$$E = E^{0'} + \frac{RT}{nF} \ln \frac{C_O}{C_R}$$

(1.3)

where E is the applied potential and $E^{0'}$ is the formal potential of the overall reaction. T denotes absolute temperature, R is the universal gas constant, F is Faraday constant, n is the number of transferred electrons in the reaction, and C_o and C_R are the concentrations of oxidized and reduced reagents, respectively (Suen *et al.*, 2017). The overpotential (η) is a difference between the applied potential (E) and potential under equilibrium conditions (equation 1.4).

$$\eta = E - Eeq$$

(1.4)

Commonly, the overpotential (η) is referred to a value that has to be applied to achieve a special current density, and a lower overpotential indicates better electrocatalytic ability for the target reaction. It should be noted that different current densities will be referred to different η values. Normally, the reported η should be referred to a current density, for example 10 mA cm^{-2}, indicated as η_{10} at j_{10} (Figure 8(a)).

1.4.1.2   Tafel equation and Tafel slope (b)

For industrial applications, a high overpotential (η) is usually needed to obtain a high current density. The current density and the applied overpotential can be described according to the well-known Butler–Volmer equation (Equation (1.5)) (John O'M. Bockris, Reddy, & Maria E. Gamboa-Aldeco, 2000).

$$i = i_0 \left[\exp\left(\frac{\alpha_a nFE}{RT} \right) + \exp \frac{\alpha_c nFE}{RT} \right]$$

(1.5)

Under high overpotential conditions, the Butler–Volmer equation can be simplified as equation (1.6) which is also known as the Tafel equation (Burstein, 2005).

$$i \approx i_0 \exp \frac{\alpha_a nF\eta}{RT}$$

(1.6)

By translating the Tafel equation to logarithm function form, equation (1.6) can be re-written as equation (1.7), where the exchange current density (i_0) and Tafel slope (b) can be calculated accordingly. The Tafel slope (b) can be expressed as equation (1.8), and from this one can understand that the definition of Tafel

slope (b) is ''how fast the current density increases against overpotential (η)'' and its value mostly depends on the transfer coefficient (α).

$$\log(i) = \log(i_0) + \frac{\eta}{b}$$

(1.7)

$$b = \frac{\partial \eta}{\partial \log(i)} = \frac{2.303\,RT}{\alpha F}$$

(1.8)

In this regard, a smaller Tafel slope (b) as illustrated in Figure 8b indicates that current density can increase fast with a small overpotential (η) change (i.e., fast reaction rate constant), which implies good electrocatalytic kinetics. In addition, the Tafel slope (b) provides valuable and insightful information about the mechanism of the reaction, especially for elucidating the rate-determining step. This can be very helpful for understanding the fundamental behavior between the electrocatalyst and reactant.
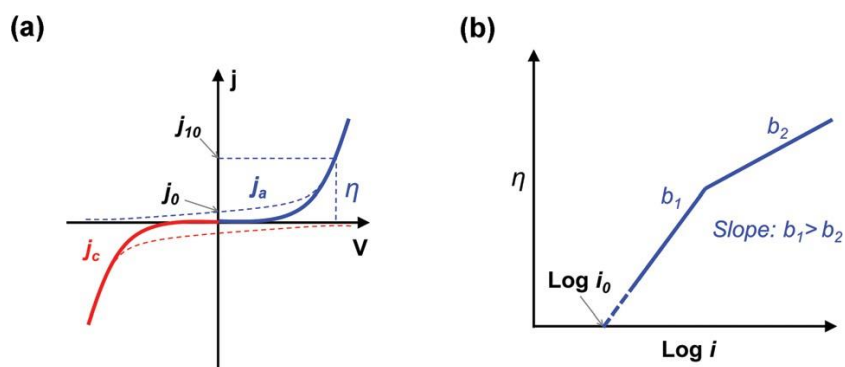
Figure 8. (a) Exemplary polarization curves for cathode (red) and anode (blue). (b) Tafel plot (Suen *et al.*, 2017).

1.4.1.3   Stability

Stability, or durability, is an important descriptor of a catalyst in view of practical application, demonstrating the ability to maintain the original activity of a catalyst over a long period of time. The stability can be evaluated by recording the variation of the overpotential at a certain current density or recording the change of current density at a fixed applied overpotential, over a period of time. It can also be evaluated by continuous cyclic voltammetric scans. Polarization curves are usually recorded before and after the stability test to make comparison. There will be an evident increase in the overpotential or decrease in the current density if the catalyst loses its activity quickly.

1.4.2 Noble metal electrocatalysts

Platinum(Pt) is well known as the best-performing catalyst for the HER, requiring negligible overpotentials to achieve high reaction rates in acidic solutions (Benck, Hellstern, Kibsgaard, Chakthranont, & Jaramillo, 2014).

Iridium oxide and ruthenium oxide are considered to be the most advanced OER electrocatalysts with relatively low overpotentials and small Tafel slopes, and have outstanding stability. (Pi, Zhang, Guo, Guo, & Huang, 2016). Many researchers have proved that the OER performance of IrO_2 is slightly worse but much more stable than RuO_2 (Cherevko *et al.,* 2016).

1.4.3 Earth-abundant transition metals electrocatalysts

Although the catalytic performance of noble metals is well recognized, the high cost and rarity are the great obstacles to their large-scale applications (Xiong, Chen, & Shi, 2018). Hence, it is desirable to develop earth-abundant and economical electrocatalysts with high HER and/or OER performance as substitutes for noble metal-based catalysts (Figure 9).
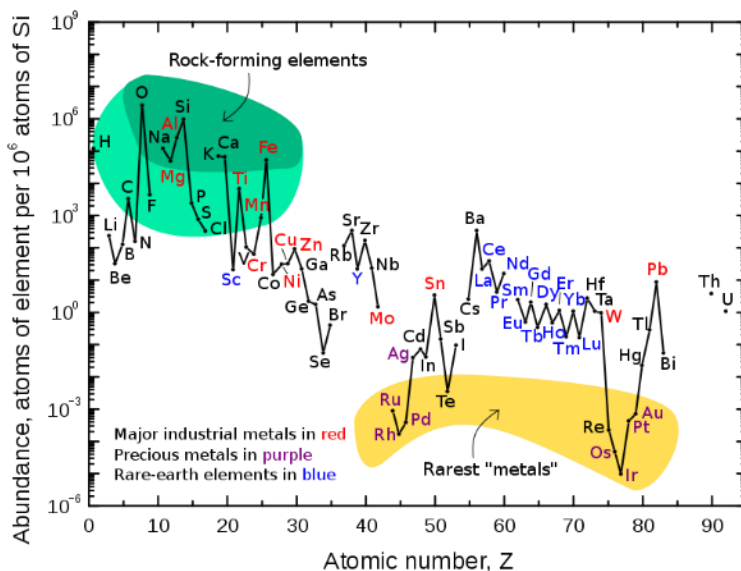
Figure 9. Abundance (atom fraction) of the chemical elements in Earth's upper continental crust as a function of atomic number (Anderson, 1983).

In the past decades, transition metal based catalysts have gained much research interest, owing to their low-cost, abundant sources and excellent corrosion resistance (Y. Zhang *et al.*, 2018). Normally, transition metal based catalysts are mainly composed of transition metal (Mn, Fe, Co, Ni, Cu, Mo and W) and non-metal

elements (O, S, Se, C, N, P), which could be divided to transition metal oxides, transition metal hydroxides/transition metal oxyhydroxides, transition metal phosphides (TMPs), transition metal sulfides, transition metal selenides, transition metal nitrides and transition metal carbides.

Among the transition metal-based catalysts, TMPs have recently received significant attention due to their excellent catalytic performance, long-term stability and bifunctionality as HER and OER catalysts in alkaline solutions.

1.4.4 Transition metal phosphide electrocatalysts

1.4.4.1 The role of phosphorus atoms

For the HER reaction of metal phosphides, TMP can be considered to dope phosphorus atoms into the crystal lattice of the transition metal. The phosphorus atom in the metal phosphide has high electronegativity and is believed to accept electrons from the metal and capture positively charged protons. Therefore, metal phosphides with increased relative phosphorus content generally exhibit an improvement in HER performance (Shi & Zhang, 2016). In addition, the activity of the phosphorus site in TMP is also related to its crystal structure. The large atomic radius of the phosphorus atom (0.109 nm) makes the metal phosphide usually a triangular prism structure, which is an anisotropic crystal structure. This structure leads to an increase in the number of unsaturated surface atoms in the metal phosphide, which promotes higher intrinsic catalytic activity (Oyama, Gott, Zhao, & Lee, 2009). For OER, metal phosphides are not promising OER catalysts theoretically. However, many efforts have been made to reveal that metal phosphide can act as a pre-catalyst and enhance catalytic activity by helping the carrier transport between the core material and the oxide (Xu, Xiong, Amorim, & Liu, 2018; Xu, Liu, *et al.,* 2018; Xu, Li, *et al.,* 2018).

1.4.4.2 Synthesis strategies of TMPs

In general, there are a variety of methods for synthesizing TMPs based on different phosphorus sources used: solution-phase, solid-state reduction, gas-solid reaction, electrodeposition and other emerging methods (Shi & Zhang, 2016; Y. Wang *et al.,* 2017).

Solution-phase reaction

The method is using trioctylphosphine (TOP) as a phosphorus source in an organic solvent at an elevated temperature (ca. 300 °C) under Ar or N_2 (Liyanage, Danforth, Liu, Bussell, & Brock, 2015). When the

temperature reaches to 300 °C, the C–P covalent bond is broken, and then different precursors such as bulk metal and metal nanoparticles (NPs), metal acetylacetonate, metal carbonyl compound and metal oxide, can be phosphatized. Different crystal phases can be obtained by adjusting the reaction temperature. Since TOP has a strong coordination effect, the rational use of TOP can effectively promote the reaction and create some unusual structures. However, the insolubility of TOP in water and its high decomposition temperature limit phosphating to only occur in high boiling organic solvents, which results in highly flammable and corrosive reactions. In addition to TOP, trioctylphosphine oxide and other organic phosphines (such as triphenylphosphine, alkyl- and aryl-phosphine) have similar effects and can be mixed with TOP as an organic phosphorus source.

Solid-state reduction

Solid phase reduction is a method mixing solid metal precursors and phosphorus source followed by thermal treatment in an inert atmosphere or under vacuum. This method is usually applied to prepare bulk MoP due to high phosphorization temperature that can break the strong Mo–O bond (Xiao *et al.,* 2014). However, it consumes considerable energy and usually obtains the bulk catalysts with few active sites.

Gas–solid reaction

The gas-solid reaction is a method in which a transition metal precursor and hypophosphite (NaH_2PO_2) or red phosphorus as a phosphorus source are placed together and then heat-treated under an inert atmosphere (Xu, Xiong, *et al.*, 2018; Xu, Liu, *et al.*, 2018; Xu, Li, *et al.*, 2018). Phosphorus source and metal precursor are placed in upstream and downstream, respectively. At certain temperatures, PH_3 produced by the decomposition of hypophosphite or phosphorus vapor released from red phosphorus can directly react with various precursors of metal oxides, hydroxides, metal organic frameworks and some other compounds to form TMPs. The greatest advantage of this method is the preservation of the morphology of the downstream precursor. In addition, the reaction is easy and free of surfactants, and the range of transition metal precursors can be used more broadly. However, it will produce highly toxic gases such as PH_3 or white phosphorus in the phosphating process, so it is necessary to evacuate these gases properly. Gas-solid reaction is used in this thesis for phosphorization.

Electrodeposition

In this method, TMPs can be grown on conductive substrates directly by reducing the metal ions and $H_2PO_2^-$ at the same time. This method can avoid phosphorization treatment at high temperatures, which alleviates the energy demand and the environmental issues of using gas-phase phosphorous sources. However, TMPs obtained from this method are generally accompanied by a high percentage of corresponding phosphates (J. Yu *et al.,* 2016).

1.4.4.3 Applications of transition metal phosphides in water splitting

To date, a number of different transition metal (e.g., Fe, Co, Ni, Cu, Mo and W) phosphides have been reported to be useful in water splitting.

Transition metal phosphides catalysts for HER

Most TMPs have excellent electrocatalytic activity for HER. They generally exhibit high intrinsic activity, good stability and approximately 100% Faraday efficiency for HER in any pH solutions. As early as 2005, the Rodriguez team firstly proposed that Ni_2P may be a good practical catalyst for HER, based on their density functional theory (DFT) calculations (Liu & Rodriguez, 2005). Nickel phosphides have a number of different polymorphs with various stoichiometry of P: Ni (i.e., NiP_x), and their electronic structure and physicochemical properties vary with composition (M. Chen, Qi, Zhang, & Cao, 2017; Huang *et al.,* 2014). Numerous studies have been conducted to gain in-depth understanding of the electrocatalytic activity of various NiP_x nanocatalysts. In 2014, X. Sun and co-workers successfully constructed NiP_2 nanosheet arrays structure on carbon cloth (Jiang, Liu, & Sun, 2014). The as-prepared NiP_2 nanosheet demonstrated superior HER performance and long-term stability for at least 57 h. Later, Dismukes *et al.* synthesized Ni_5P_4 microparticles for HER in both acidic and alkaline media, which exhibited exceptionally high HER activity with a low overpotential and a small Tafel slope in acid media. Meanwhile, their HER activity in alkaline media also outperformed that of the analogous Ni_2P nanocrystals (Laursen *et al.,* 2015). Furthermore, Liu et al. carefully compared HER activity of NiP_x with different ratios, and found that Ni_5P_4 crystals showed much higher electrocatalytic activity than $Ni_{12}P_5$ and Ni_2P for HER in acid solution. The reason could be attributed to the higher positive charge of Ni and a stronger ensemble effect of P in Ni_5P_4 (Pan *et al.,* 2015). Apart from the single-phase nickel phosphides mentioned above, the electrocatalytic properties of Ni_5P_4-Ni_2P nanosheet arrays have been studied by Liu and co-workers. The Ni_5P_4-Ni_2P nanosheet showed a low onset overpotential and excellent long-term durability in acidic solution (X. Wang, Kolen'ko, Bao, Kovnir, & Liu, 2015).

Besides nickel phosphides, different cobalt phosphide nanostructures were also explored as HER catalysts. Schaak's group firstly prepared uniform cobalt phosphide NPs with an average particle size of 13 ± 2 nm supported on a Ti foil with good HER performance in acid media (Popczun, Read, Roske, Lewis, & Schaak, 2014). After that, improved electrocatalytic activity was realized on the cobalt phosphide nanowires in a wide pH range from 0 to 14 (Tian, Liu, Asiri, & Sun, 2014). Inspired by the advantages of two-dimensional materials, Zhang et al. synthesized porous CoP nanosheets with a thin thickness of 1.1 nm. The as-prepared samples present a high proportion of CoP (200) crystal face, which have been theoretically regarded to be highly active toward the HER. As expected, the porous CoP nanosheets delivered super electrocatalytic performance, with a low overpotential, a small Tafel slope in acid media and long-term durability of over 24 h in the time-dependent current density test (C. Zhang *et al.,* 2017).

Meanwhile, iron phosphide (FeP_x) is also considered to be highly active toward the HER. FeP, Fe_2P and Fe_3P have been demonstrated to exhibit good HER activity. Whitmire et al. synthesized phase-pure Fe_xP (x = 1, 2, 3) thin films to study and compare their catalytic activities, and they observed that the HER activity increased in the order of FeP < Fe_2P < Fe_3P (Schipper *et al.,* 2018). Additionally, FeP NPs with uniform hollow sphere structure (Callejas *et al.,* 2014) and nanowire morphology (Jiang, Liu, Liang, *et al.,* 2014) were prepared for HER in different electrolytes. In addition to the phosphide catalysts mentioned above, Cu_3P (Han, Zhang, Yuan, Ji, & Du, 2017), MoP (Xiao *et al.,* 2014), and WP (McEnaney *et al.*, 2014) were also reported to exhibit good HER activity.

Transition metal phosphides catalysts for OER

Metal phosphides have been reported as OER electrocatalysts dating back to the 1990s. Kupka et al. (Kupka & Budniok, 1990) obtained an amorphous Ni-Co-P alloy by first galvanostatic electrodeposition, followed by further heat treatment at 500 °C to convert the amorphous alloy to a crystalline Ni-Co-P alloy. It has also been found that Ni-Co-P alloys are oxidized on their surfaces to form oxyhydroxides, which may have a specific effect on electrocatalysis. After that, the study of metal phosphides seems to be very frustrating. Until 2015, Yoo *et al.* (Ryu, Jung, Jang, Kim, & Yoo, 2015) made remarkable progress, showing that the true catalytic site of metal phosphide is not the bulk phosphide but the surface oxidized species. Followed by this work, metal phosphide based OER catalysts have been extensively investigated in the past few years.

Cobalt-based phosphides have been demonstrated to show good activity for OER. Zhu *et al.* (Zhu, Liu, Ren, & Yuan, 2015) used electrodeposition to fabricate well-defined mesoporous CoP nanorod arrays on Ni foam with good OER activity, and they also found the cobalt presented higher oxidation state than 2. In addition, Wang et al. (P. Wang, Song, Amal, Ng, & Hu, 2016) reported CoP-based nanoneedle arrays supported on carbon cloth as a highly active catalyst for both OER and HER, and found that the nanoarray morphology has a significant contribution to the activity. Liu *et al.* developed a hollow octahedron phosphide electrocatalysts for OER through *in-situ* phosphorization of cobalt oxide octahedron and subsequent etching in acid (Xu, Liu, *et al.,* 2018). All these nanostructures of cobalt phosphides show efficient catalytic ability due to their high specific surface area and superior charge transferability.

Similar to cobalt phosphide, nickel and manganese based phosphides such as NiP, Ni_2P, MnP and CoMnP were also investigated for OER. Yu et al. fabricated carbon-coated porous nickel phosphides nanoplates with Ni_2P and Ni_5P_4 mixed phases (X. Yu *et al.*, 2016). The NiO and $Ni(OH)_2$ porous nanoplates with a similar morphology were also fabricated for comparison. The results showed that nickel phosphide exhibits much better activity and higher stability. Meanwhile, Stern et al. showed that Ni_2P NPs was an excellent OER catalyst in 1 M KOH (Stern, Feng, Song, & Hu, 2015). Meanwhile, Liu *et al.* reported a series of nanoparticulate phosphides containing different equimolar metal (M = Fe, Co, Ni) components and systematically explored how the compositions influenced the OER activities. A notable trend in OER activity was observed, following the order of FeP < NiP < CoP < FeNiP < FeCoP < CoNiP < FeCoNiP, which indicate that the introduction of a secondary metal(s) to a mono-metallic TMP substantially boosts the OER performance (Xu, Liu, *et al.,* 2018).

1.4.5 Strategies for improving electrocatalytic performance

Generally, there are two major strategies to improve the performance of an electrocatalyst, as shown in Figure 10:

i. Increasing the number of active sites on a given electrode via altering the morphology of catalysts or loading active catalysts on a special support etc.;
ii. Increasing the intrinsic activity of each active site via altering the catalyst's composition or electronic structure etc.

It should be noted that these strategies not mutually exclusive and can ideally be addressed simultaneously, leading to great improvements in activity (She *et al.*, 2017). Specifically, for TMPs based catalysts there are

several methods to improve their performance, including composition engineering, structure engineering, and supporting TMPs on a 3D substrate, etc.
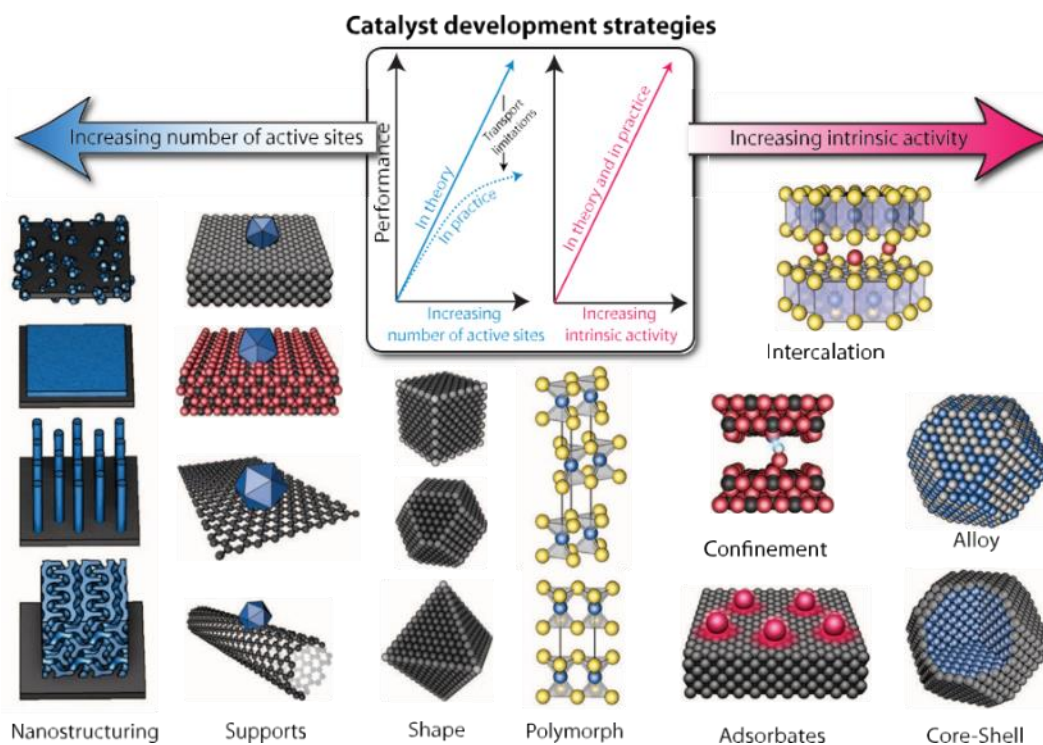
Figure 10. Catalyst development strategies (She *et al.*, 2017).

Composition engineering

Doping or alloying with metal or non-metal elements in mono-phase catalysts has become an efficient approach to preparing catalysts with enhanced HER or OER performance. Doping or alloying can effectively tune electronic structures and optimize the absorption energy of intermediates produced in HER or OER, and thus substantially improve intrinsic catalytic properties of catalysts. For example, the HER efficiency of CoP can be promoted by doping other metal elements like Fe and Ni (Cabán-Acevedo *et al.*, 2015; Liang *et al.*, 2016) or some other non-metal elements. Certainly, this doping strategy can be applied to other metal phosphides with other dopants.

Structure engineering

The catalytic activities of TMPs are not only determined by their composition but also affected by their morphology and structure. As the catalytic reactions always take place on the surface of the catalysts,

preparing porous nanostructures is an effective means to improve the catalytic performance of catalysts. The porous structure presents a large specific surface area that provides more catalytically active sites exposed to the electrolyte and promotes mass transfer and interface charge carrier exchange (Wu, Pi, Zhang, & Chen, 2016).

Supported-TMPs

Supporting TMPs on a conductive support is also an effective strategy to improve catalytic performance. For example, TMPs/nano-carbon composites or TMPs on 3D metal foam enable to achieve higher catalytic performance than unsupported TMPs. The introduction of nano-carbon or 3D metal foam here can not only improve the electrical conductivity of the hybrid, but also provide an enhanced specific surface area to allow more active sites to be exposed.

Chapter 2. Objectives

This chapter lists the objectives of this thesis, which are based on the development of cobalt-based TMP to be used as catalysts for the oxygen evolution reaction and hydrogen evolution reaction.

Developing high-performance, low-cost, and durable electrocatalyst is of critical importance for widespread deployment of water splitting devices. The main objective of this work is to study and develop advanced earth-abundant materials as substitutes of platinum-group metals for water splitting. As per performance improvement strategies discussed in Chapter 1, doping and supporting strategies will be chosen to improve the water splitting performance of Co-based electrocatalysts.

Specifically, to increase the intrinsic catalytic performance of CoP, Ni will be doped/mixed into CoP nanoparticle catalysts, and the research aims:

❖ To develop a simple and low-cost method to prepare Ni doped CoP, i.e., CoNiP catalysts;

❖ To carry out comprehensive physicochemical characterization using a range of advanced materials characterization techniques including X-ray Diffraction (XRD), Transmission Electron Microscopy (TEM), and X-ray Photoelectron Spectroscopy (XPS);

❖ To test the electrocatalytic performance of the obtained CoNiP catalysts toward the oxygen evolution reaction (OER), hydrogen evolution reaction (HER), and overall water splitting (OWE), using cyclic voltammetry (CV) and galvanostatic electrolysis (GE), and to compare it to that of the state-of-the-art control catalysts (i.e. RuO_2, Pt/C);

❖ To investigate the reaction kinetics using Tafel analysis.

To increase the catalytic current density in a given surface area of electrode, supported CoP catalysts, namely, self-supported porous CoP foam will be developed in this thesis. The research aims:

❖ To obtain hierarchical porous structure by performing electrochemical anodization of 3D macroporous Co foam;

❖ To convert anodized Co foam into CoP and optimize the phosphorization conditions according to the results of electrocatalytic tests;

❖ To comprehensively characterize the obtained porous CoP foam using a range of advanced materials characterization techniques including Scanning Electron Microscopy (SEM), X-ray Diffraction (XRD), Transmission Electron Microscopy (TEM), and X-ray Photoelectron Spectroscopy (XPS);

❖ To investigate the electrocatalytic performance of the porous CoP foam toward the OER, HER, and OWE, using electrochemical techniques of CV and GE;

❖ To study how the pH values of the electrolyte influences the electrocatalytic performance, and how the porous CoP foam behaves at high catalytic current densities.

Chapter 3. Experiment

This chapter addresses the materials, instruments and methods used in this thesis. Detailed experimental procedures and methods are given, including the preparation of the catalysts, material characterization and electrochemical characterization.

3.1 Samples and materials

3.1.1 Catalysts

In this thesis, two types of catalysts are synthesized: one is powdery CoNiP nanoparticles (NPs) and another one is self-supported porous CoP foam. The optical photographs of these two catalysts are shown in Figure 11 a) and 11 b), respectively.
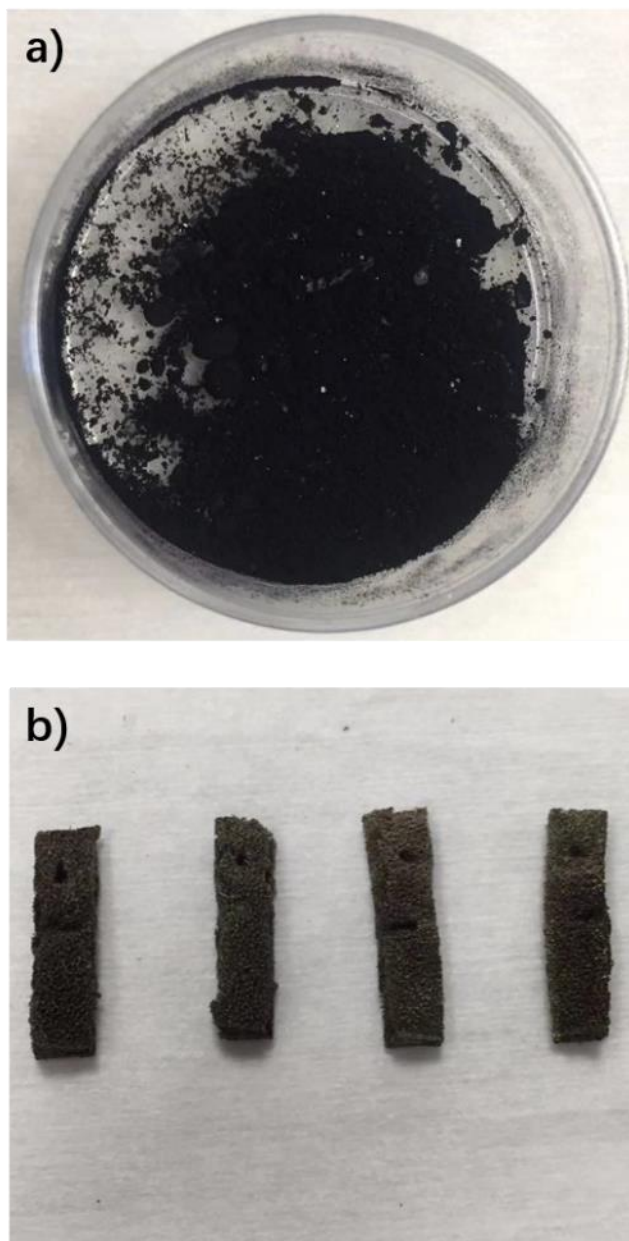
Figure 11. Optical photographs showing the appearance of a) CoNiP NPs. b) Porous CoP foam.

3.1.2 Chemicals and Materials

The chemicals and materials used in this work are listed in Tables 3 and 4. All materials were used as received without any further purification. Deionized (DI) water from a Millipore system (18.2 MΩ cm) was used for solution preparation.

Table 3. The chemicals used in this thesis work.

Chemicals	Formula	Purity	Manufacturer
Cobalt (II) chloride 6-hydrate	$CoCl_2.6H_2O$	98%	Panreac Quimica SLU, Spain
Nickel (II) chloride hexahydrate	$NiC_{l2}. 6H_2O$	98%	Acros Organics, German
Ethanol	C_2H_5OH	99%	Honeywell
Acetone	C_3H_6O	99%	Sigma-Aldrich
Sulfuric acid	H_2SO_4	97.5%	Sigma-Aldrich
Sodium nitrate	$NaNO_3$	99%	Sigma-Aldrich
Potassium permanganate	KMO_4	99%	Sigma-Aldrich
Hydrogen peroxide solution	H_2O_2	30wt%	Sigma-Aldrich
Sodium hypophosphite monohydrate	$NaBH_4$	99%	Sigma-Aldrich
Ethylene glycol (EG)	$C_2H_6O_2$	99.8%	Sigma-Aldrich
Glycerol (GC)	$C_3H_8O_3$	99%	Sigma-Aldrich
Ammonium fluoride	NH_4F	99%	Sigma-Aldrich
Nafion solution	/	5 wt%	Sigma-Aldrich
phosphorus red	P	97%	Sigma-Aldrich
Ruthenium oxide, anhydrous	RuO_2	99.9%	Alfa Aesar
Commercial Pt/C	/	20 wt%	Fuel cell store, USA

Table 4. The materials used in this thesis work.

Materials	Specification	Manufacturer
Cobalt foam (CF)	1.0 mm thick, 110 Pores Per Inch	Heze Jiaotong Group, China
Carbon paper (CP)	SpectracarbTM 2050A-0850	Fuel cell store, USA

3.2 Preparation of CoNiP NPs

The CoNiP NPs were prepared by chemical reduction of the corresponding cobalt and nickel cations in the presence of $NaBH_4$ in ethylene glycol (EG) solution and subsequent phosphorization using NaH_2PO_2 as the phosphorus source. All the processes are summarized in the schematic diagram as shown below in Figure 12:
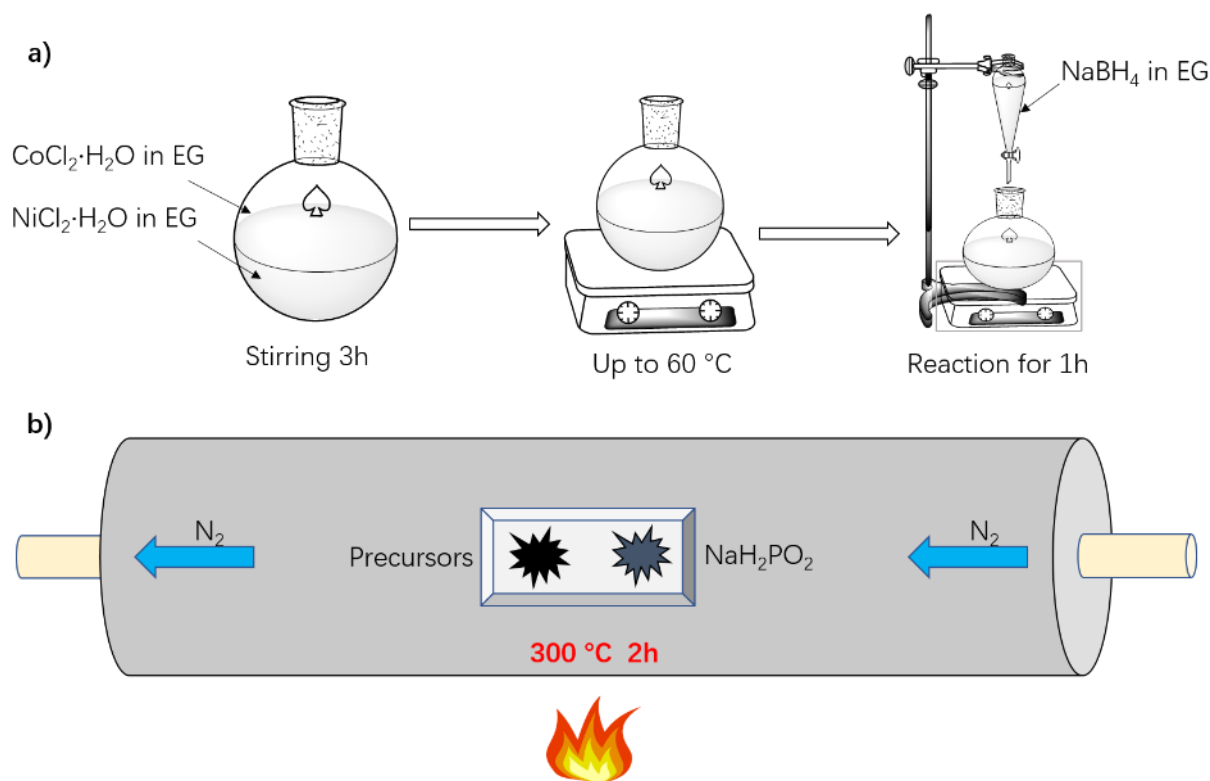
Figure 12. CoNiP NPs preparation processes. a) Preparation of precursor. b) Phosphorization.

3.2.1 Preparation of precursor

Briefly, the EG solutions of $CoCl_2 \cdot 6H_2O$ (10.0 mL, 0.05 M Co^{2+}) and $NiCl_2 \cdot 6H_2O$ (10.0 mL, 0.05 M Ni^{2+}) were mixed, held at 25 °C under magnetic stirring for 3 h. Next, the solution temperature was increased to 60 °C and $NaBH_4$ solution (30 mL, 10 mg mL^{-1}) was slowly added under rigorous stirring. After reaction for 1 h, the mixture was cooled down to 25 °C, centrifuged and rinsed several times with DI water. The as-obtained powders were dried in a vacuum oven at 80 °C for 24 h.

3.2.2   Phosphorization

The phosphorization was performed at 300 °C using NaH_2PO_2 as the source of phosphorus. Typically, 0.1 g of catalyst powders was loaded in a ceramic boat, with 0.5 g of NaH_2PO_2 placed 2 cm away from the precursors at the upstream side. Subsequently, the boat was put into a tube furnace, wherein high-purity N_2 (99.999%) was purged at a flow rate of 800 SCCM for 1 h to remove air. Afterwards, the furnace was ramped to 300 °C at a rate of 5 °C min^{-1}, held at this temperature for 2 h, and then cooled down naturally to room temperature. A constant N_2 flow was maintained in the whole process. Finally, the CoNiP NPs were obtained.

3.3 Preparation of porous CoP foam

The porous CoP foam was obtained using electrochemical anodization, followed by thermal annealing and subsequent phosphorization using red phosphorus as the phosphorus source. All the processes are summarized in the schematic diagram as shown below in Figure 13:
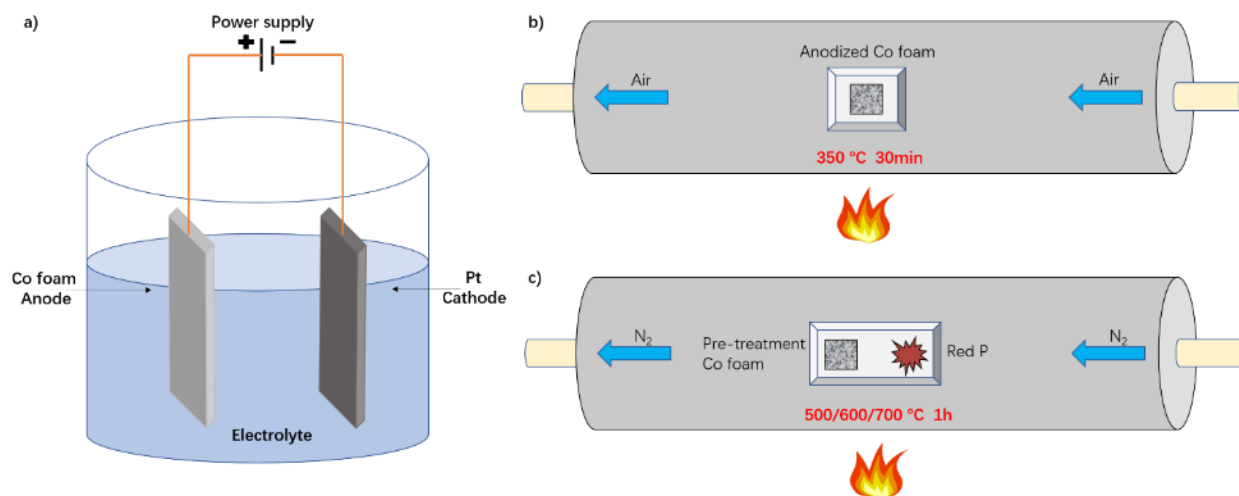
Figure 13. Porous CoP foam preparation processes. a) Electrochemical anodization. b) Thermal annealing c) Phosphorization.

3.3.1   Electrochemical anodization

The substrates of commercial CF (20 mm × 10 mm ×1 mm) were cleaned via ultrasonication in acetone and ethanol successively, followed by rinsing with DI water and drying the samples in a nitrogen stream. Electrochemical anodization was performed at a constant voltage of 50 V for 4 h below 5°C in a mixed EG

and GC solvent (volume ratio of 1:3) containing 3 M DI water and 0.54 M NH_4F. The samples were then rinsed with DI water and dried under nitrogen gas flow. Electrochemical anodization was performed using a Keithley 2400 source meter in a two-electrode configuration with a counter electrode made of platinum wire. A temperature-controlled thermostat (Huber, Germany) with a cooling plate and ice bath was used to effectively control the temperature.

3.3.2 Thermal annealing

The annealing of the anodized samples was performed at 350 °C for 30 min in a tube furnace (Carbolite) in air.

3.3.3 Phosphorization

To convert the porous Co oxide to a porous Co phosphide, post-phosphorization was performed using red P as the phosphorus source. Typically, 1 piece of pre-treated CF was loaded in a ceramic boat, with 1 g of red P placed 2 cm away from the precursors at the upstream side. The boat was put into a tube furnace (Carbolite), wherein high-purity N_2 (99.999 %) was used the carriage gas purged at a flow rate of 500 mL/min for 1 h to remove air. Afterwards, the furnace was ramped to 500, 600 or 700 °C at a rate of 10 °C min^{-1}, held at this temperature for 1 h, and then cooled down naturally to room temperature. A constant N_2 flow was maintained in the whole process.

3.4 Material Characterization

XPS, XRD, SEM and TEM were applied to study the microstructure, morphology, and composition of the catalysts. The detailed description of these techniques is summarized in this section.

3.4.1 X-ray Diffraction (XRD)

XRD is a non-destructive technique for analyzing the phase composition and structure of materials. It primarily works for materials that are crystalline or at least partially crystallized (i.e., that have periodic structural order), but it is sometimes also used to study non-crystalline materials. XRD is the elastic scattering of X-ray photons by atoms in a periodic lattice. The scattered monochromatic X-rays that are in phase give

constructive interference. Figure 14 illustrates how diffraction of X-rays by crystal planes allows one to derive lattice spacing by using the Bragg's law.

$$n\lambda = 2d\sin\theta \qquad\qquad (3.1)$$

where n is an integer called the order of reflection, λ is the wavelength of X-rays, d is the characteristic spacing between the crystal planes of a given specimen and θ is the angle between the incident beam and the normal to the reflecting lattice plane. By measuring the angles, θ, under which the constructively interfering X-rays leave the crystal, the interplanar spacing, d, of every single crystallographic phase can be determined (Chatterjee, 2001).
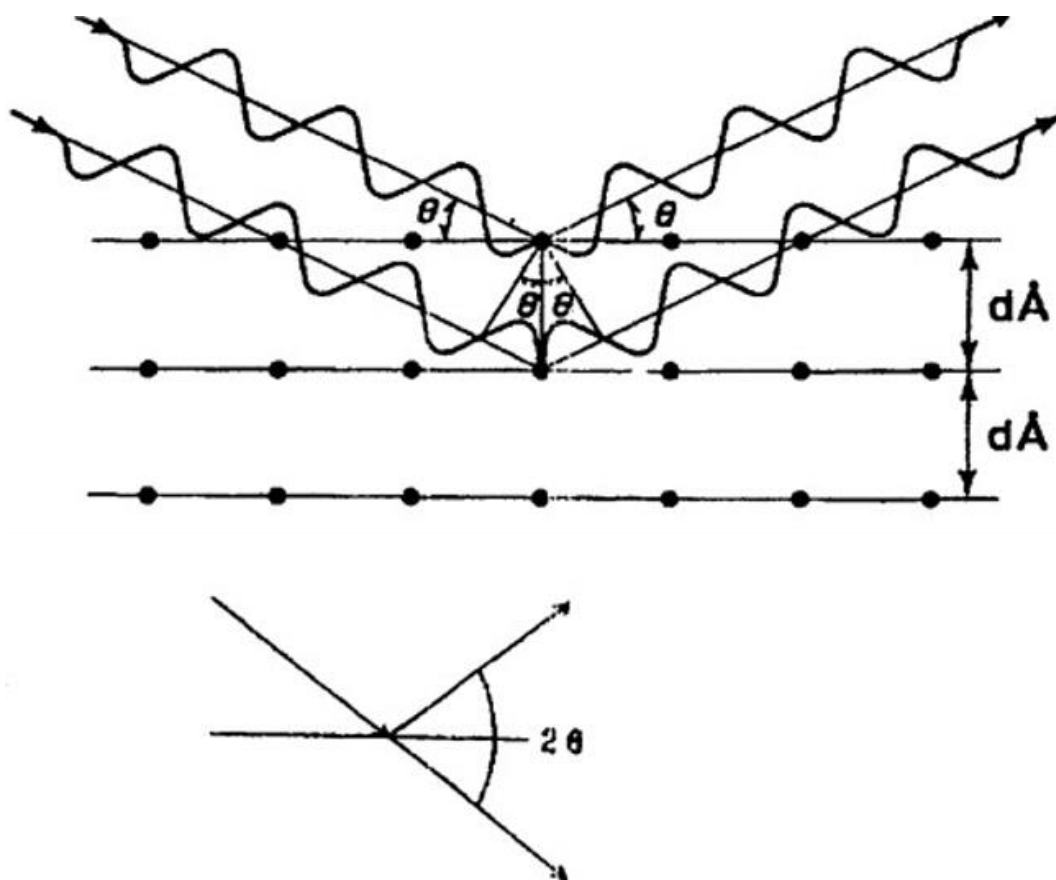
Figure 14. Schematic representation of the Bragg's Law (Chatterjee, 2001).

The experiment data are compared with the standard line patterns available for various compounds in the Powder Diffraction File (PDF) database. This file is released and annually updated by the International Centre for Diffraction Data (ICDD). It contains line patterns of more than 60,000 different crystallographic phases.

In practice, for any unknown sample, the appearance of three most intense characteristic lines from the standard PDF line pattern is sufficiently convincing evidence of the existence of a crystalline phase in either a homogeneous substance or even in a multicomponent mixture. In some cases, a distinction between two or more possible phases can be done by comparing the other characteristic lines. Furthermore, prior knowledge of the class of materials under investigation and the chemical analysis data can be of great value.

In this thesis, XRD experiments were conducted on a X'Pert PRO diffractometer (PANalytical) set at 45 kV and 40 mA, using Cu Kα radiation (λ = 1.541874 Å) and a PIXcel detector (Figure 15). Data were collected with the Bragg-Brentano configuration in the 2θ range of 10° – 90° at a scan speed of 0.01° s^{-1}. The results were analyzed using Highscore software (PANalytical) with a standard reference of Cryst50.

Figure 15. X'Pert PRO diffractometer (PANalytical) used in this thesis work.

3.4.2 X-ray Photoelectron Spectroscopy (XPS)

XPS is a very powerful technique for elemental and chemical analysis of materials. It uses the incident monoenergetic X-rays (typically Mg Kα or Al Kα) to excite electrons from the surface atoms. The energy of these electrons can then be measured in the hemispherical detector for further analysis. The high vacuum operating conditions of XPS instrument benefit in increment of mean free path of emitted electrons. Increased mean free path of emitted electrons minimizes any energy losses resulting in better precision on elemental analysis. Energy of the incident X-ray beam (hν) is 1253.6 or 1486.6 eV for Mg Kα and Al Kα, respectively, and the kinetic energy of emitted electrons (EK) is measured and a correction is made for the work function

of the solid (EW) for the measurements of the characteristics binding energy (EB) values for an element present on the surface as given by the equation (3.2) (Verma, 2007):

$$EK = h\nu - EB - EW \qquad\qquad (3.2)$$

Figure 16 shows the basic components of a monochromatic XPS system. XPS is a surface sensitive technique which can measure approximately 10 nm depth from the surface. The incident X-rays can penetrate up to few micrometers of the sample, but the emitted electrons from these regions cannot escape from more than 10 nm depth to provide characteristics information as they travel to the surface of the material. Other advanced techniques such as depth profiling for measuring the bulk or near surface properties have been integrated with modern XPS instrument. It relies on the principle of etching the surface over time using a mini beam source and then measuring the surface as normal XPS technique. The same analysis area is etched several times until the substrate's elemental properties are revealed within the XPS measurements.
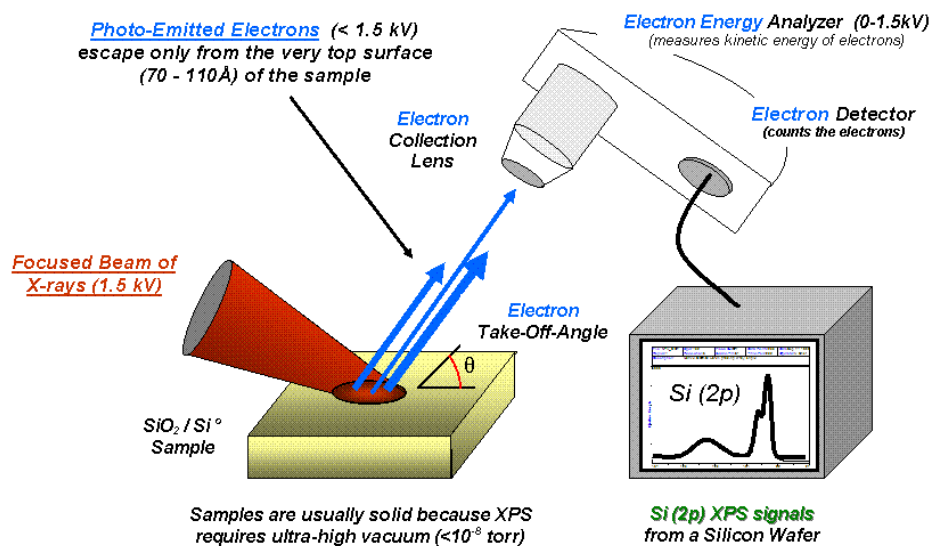
Figure 16. Basic components of a monochromatic XPS system (Wikipedia contributors, 2011).

In this work, XPS data were acquired on an ESCALAB 250Xi X-ray photoelectron spectrometer (Thermo Scientific) using Al Kα radiation (1489.6 eV, Figure 17).

Figure 17. ESCALAB 250Xi X-ray photoelectron spectrometer (Thermo Scientific) used in this thesis work.

3.4.3 Scanning Electron Microscopy (SEM)

SEM is one of the most widely used methods for characterizing the morphology of micro-/nano-strutured materials. Both the optical microscopy and scanning electron microscopy techniques are analogous and share some common principles such as magnification, illumination of light (optical microscopy) or electrons. In SEM technique, sample is probed using a beam of electrons rather than visible light that is used in optical microscopy. At any given time, a single source of energy from an electron gun source is collimated and focused on the sample using magnetic lenses. SEM is widely used in morphological and elemental characterizations for samples obtained from a variety of fields such as biology, geology, chemistry, physics etc. (Reichelt, 2007).
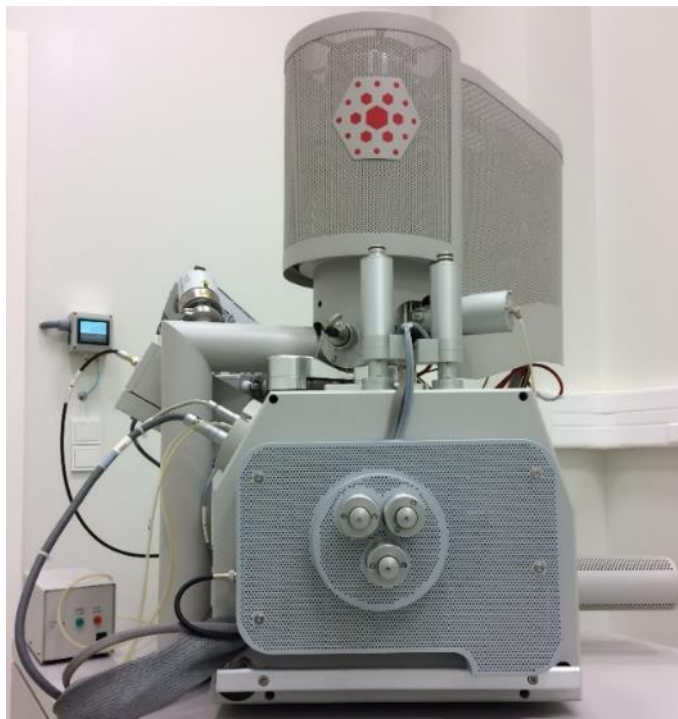
Figure 18. FEI Quanta 650 FEG microscope used in this thesis work.

SEM examination in this work was performed on a FEI Quanta 650 FEG microscope equipped with INCA 350 spectrometer (Oxford Instruments) for EDS (Figure 18). The sample surface was scanned with an electron beam and the emitted electrons from the sample were collected by a secondary electron detector.

3.4.4 Transmission Electron Microscopy (TEM)

TEM is a microscopic technique in which a powerful beam of electrons is transmitted through a specimen of a sample for characterization. The specimen needs to be less than approximately 100 nm thick to obtain distinguishable lattice within the sample. TEM characterization also uses electrons like the SEM imaging technique. However, in a TEM measurement, the whole sample is illuminated at once and the bulk (interior) is imaged, instead of only near surface imaging via single pixel SEM measurement. As the electron beam is transmitted through the specimen, image is magnified and focused onto an imaging screen or a charge-coupled device (CCD) camera. The transmitted electrons can provide much information on crystallographic orientation, lattice space of atoms. In addition, X-rays generated by the electrons can provide elemental

composition of the specimen. Compared to SEM, a much more energetic electron beam (120-200 kV) is needed to pass through the specimen in TEM providing all the possible information (Williams & Carter, 1996).

In this work, TEM was performed by high resolution TEM (HRTEM) (Figure 19) and scanning transmission electron microscopy (STEM) investigations were carried out on a probe-corrected transmission electron microscope operating at 200 kV (FEI Themis 60 – 300).

Figure 19. Double Corrected HRTEM - Titan Themis 60-300 kV used in this thesis work.

3.5 Electrochemical characterization

The electrocatalytic performance of the catalysts was accessed via cyclic voltammetry (CV) and the catalytic stability was evaluated by galvanostatic electrolysis (GE). The detailed description of these techniques is summarized below in this section.

3.5.1 Cyclic voltammetry (CV)

CV is a potentiodynamic electrochemical measurement that is most commonly employed to observe qualitatively the characteristics of an electrocatalyst. This technique sweeps a potential from an initial potential to an end potential, from where the potential is cycled back to the starting potential. In this

experiment, the potentiostat measures the current resulting from the change in applied potential against the reference electrode which controls the potential. The presence of a peak current response reveals electrochemical reactions at the working electrode/electrolyte interface at a certain applied potential.

CV often gives a pair of redox peaks, called oxidation and reduction peaks for a reversible redox reaction. Figure 20 shows a typical CV response of reversible redox couple during a single potential cycle.
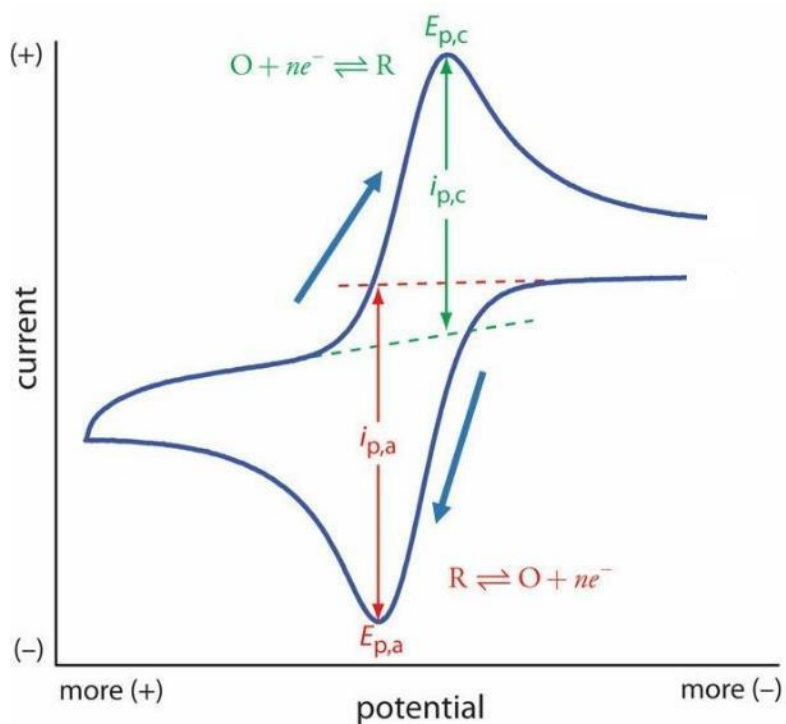
Figure 20. Cyclic voltammogram showing the measurement of the peak currents and peak potentials (David Harvey, 2000).

For the first half, a negative going potential scan is chosen from a value where no reduction occurs because O is in the oxidized form initially. As the applied potential approaches, the characteristic E° for the redox process, a cathodic current peak is observed due to O + e⁻ ↔ R. During the reverse scan, R molecules are re-oxidized back to O with an anodic peak that is characteristic of oxidation R ↔ O + e⁻.

3.5.2 Galvanostatic electrolysis(GE)

GE, also is known as constant current electrolysis, is the measurement of time depended potential at a constant current density. It is the most frequently used strategies for stability evaluation (Yan *et al.*, 2018).

3.5.3 Electrode preparation

3.5.3.1   Electrode of CoNiP NPs

The preparation of the CoNiP NPs electrode is schematically shown in Figure 21. Firstly, the catalyst ink was prepared by ultrasonically dispersing 5 mg of CoNiP powder into 1 mL of ethanol containing 50 μL of Nafion$^{®}$ solution. To prepare an electrode for catalytic tests, 70 μL of catalyst ink was loaded on a CP with an area of 1 cm^2, leading to a loading density of ca. 0.3 mg cm^{-2}. The electrode was then dried at room temperature (ca. 25 °C) naturally in air. The electrode is shown in Figure 22 a.
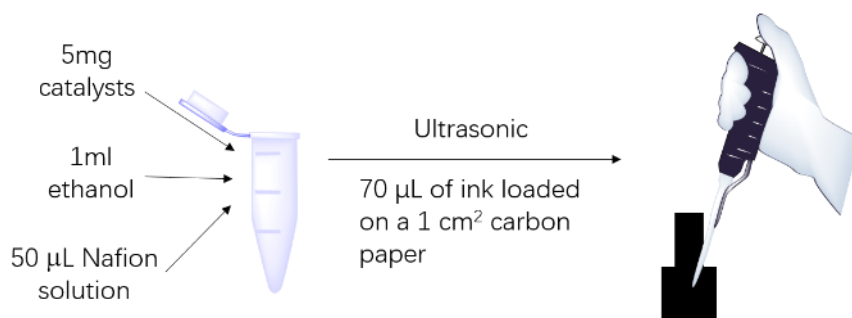
Figure 21. The schematic illustration of the CoNiP NPs electrode preparation.

The catalyst loading can be calculated as follows:

C = 5 mg × (70μL / (1000 μL + 70 μL)) / 1 cm^2 = 0.3 mg cm^{-2}

where C represents the loading mass of catalysts.

3.5.3.2   Electrodes of porous CoP foam

The as-fabricated porous CoP foam with an exposed area of either 0.5 or 0.25 cm^2 was directly used as the working electrode, as shown in Figure 22b.
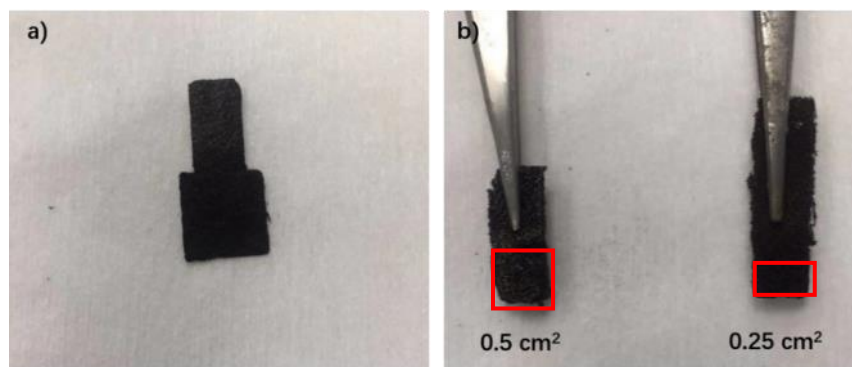
Figure 22. a) CoNiP NPs loaded on the 1 cm^2 CP. b) Porous CoP foam electrode with an anodized area of 0.5 and 0.25cm^2.

3.5.4 Electrocatalytic tests

All electrochemical measurements were conducted at room temperature (ca. 25 °C) using a Biologic VMP-3 potentiostat/galvanostat in a typical three-electrode configuration for the HER and the OER tests or a two-electrode configuration for OWE, as shown in Figure 23.

3.5.4.1 OER electrocatalytic tests

For OER performance, the catalyst-loaded CP or as-fabricated porous CoP foam, a Pt wire and a saturated calomel electrode (SCE) were utilized as working, counter, and reference electrodes, respectively. 1.0 M KOH was used as the electrolyte. The SCE reference was calibrated prior to each measurement in pure H_2-saturated 0.5 M H_2SO_4 solution using a clean Pt wire as the working electrode. Unless otherwise stated, all potentials are reported versus the reversible hydrogen electrode (RHE) by converting the measured potentials according to the following equation:

$$E_{RHE} = E_{SCE} + 0.059 \times pH + 0.244 \qquad (3.3)$$

CV was performed at a scan rate of 5 mV s^{-1} in 1.0 M KOH. *iR*-correction (85%) was made to compensate for the voltage drop between the reference and working electrodes, which was measured by a single-point high-frequency impedance measurement. The correction was done according to the following equation:

$$E_{corr} = E_{mea} - iRs \qquad (3.4)$$

where E_{corr} is iR-corrected potential, E_{mea} experimentally measured potential, and R_s the resistance from the single-point high-frequency impedance measurement.

The stability of catalysts was assessed using GE is at a constant current density. All CVs and GE curves were recorded in the electrolyte constantly bubbled with O_2.

3.5.4.2 HER electrocatalytic tests

For HER performance, a catalyst-loaded CP or an as-fabricated porous CoP foam, a graphite rod and a SCE were utilized as working, counter, and reference electrodes, respectively. The SCE reference was calibrated prior to each measurement in pure H_2-saturated 0.5 M H_2SO_4 solution using a clean Pt wire as the working electrode. Unless otherwise stated, all potentials are reported versus RHE by converting the measured potentials according to the equation (3.3).

CV was performed at a scan rate of 5 mV s^{-1} in both 0.5 M H_2SO_4 and 1.0 M KOH. *iR*-correction (85%) was made to compensate for the voltage drop between the reference and working electrodes, which was measured by a single-point high-frequency impedance measurement. The correction was done according to the equation (3.4).

The stability of catalysts was assessed using GE at a constant current density. All CVs and GE curves were recorded in the electrolyte constantly bubbled with Ar/H_2 (5% H_2, v/v).

3.5.4.3 Overall splitting tests

For OWE, a symmetrical full electrolyzer was constructed using two identical electrodes as cathode and anode, respectively. OWE performance and stability were evaluated using CV and GE in a two-electrode configuration in 1.0 M KOH. CV curves were recorded at a sweep rate of 2 mV s^{-1}. All CV and GE curves are obtained both with and without *iR*-correction in a two-electrode configuration.
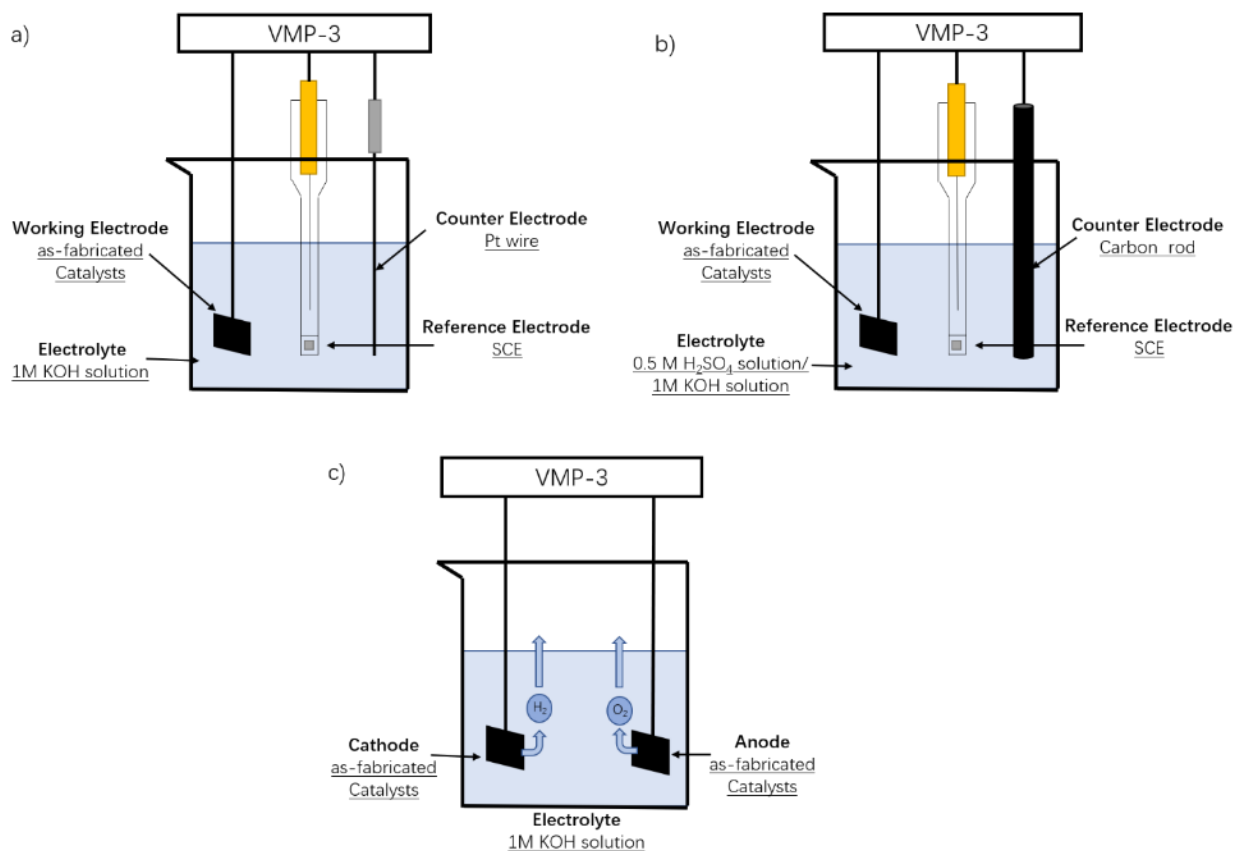
Figure 23. Schematic illustration of the three-electrode configuration for a) the OER, b) HER tests, and c) the two-electrode configuration for OWE tests.

Chapter 4. Results and Discussion

This chapter presents and discusses all the results obtained throughout the development of the experimental work. The morphology, nanostructure and electrocatalytic performance of the as-prepared two types of catalysts in chapter 3 are presented in detail.

4.1 CoNiP NPs as catalysts for water splitting

4.1.1 Morphology and nanostructure

The crystalline structure of as-prepared CoNiP NPs was firstly examined by XRD. As shown in Figure 24, the as-obtained CoNiP NPs consist exclusively of hexagonal phase-pure CoNiP (ICDD No. 04-001-4562). The characteristic peaks located at 40.9°, 44.8°, 47.5°, 54.4°, 54.7°, 55.3°, 73.1° and 75.3° can be assigned to the diffractions of (111), (201), (210), (300), (002), (211), (311) and (212) crystal planes, respectively.
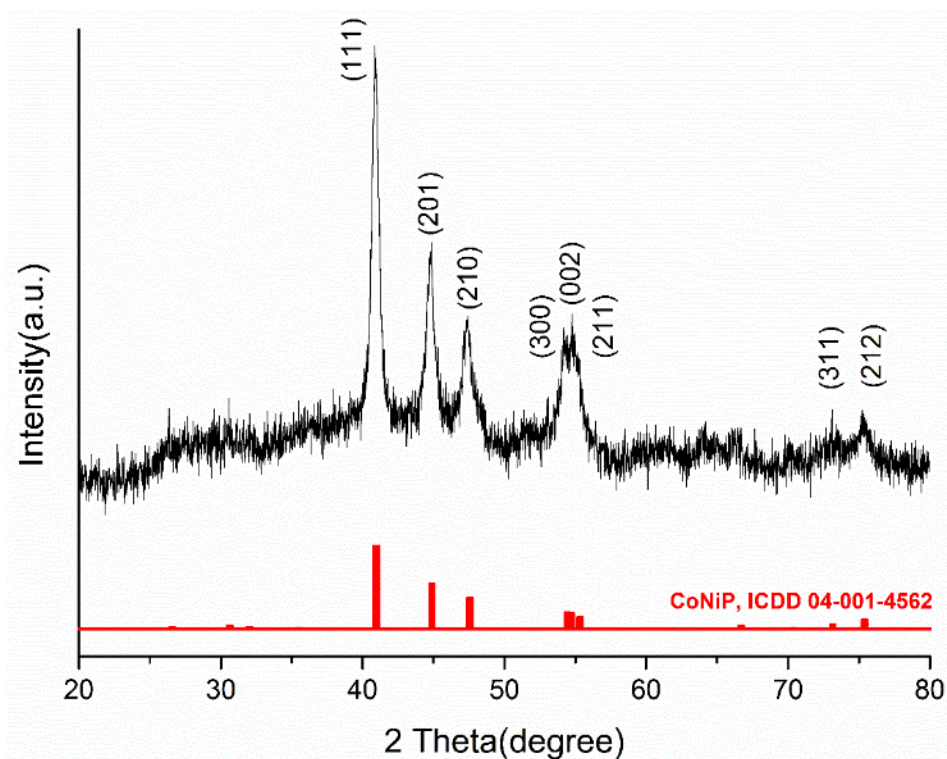
Figure 24. XRD pattern of CoNiP NP catalysts. For comparison, the standard diffraction pattern of hexagonal CoNiP (ICDD 04-001-4562) is given.

The morphology, microstructure and composition of as-prepared CoNiP NPs were further examined by TEM characterization. TEM observation (Figure 25a) revealed that the NPs comprise aggregates of small CoNiP NPs with a narrow particle size distribution (5-10 nm), which was further confirmed by high-magnification TEM imaging (Figure 25 b).
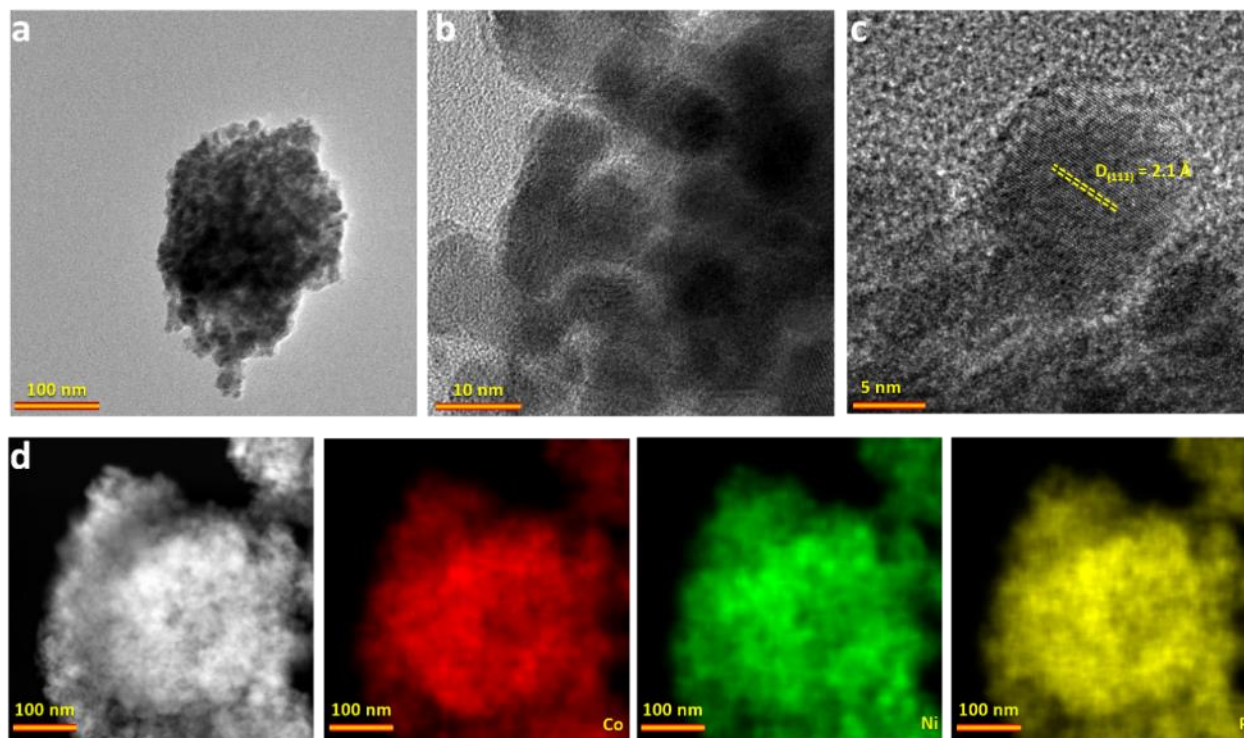
Figure 25. Microstructural and compositional characterization of CoNiP NPs catalysts. (a, b) TEM images at different magnifications, (c) HRTEM, (d) HAADF image and elemental maps of Co, Ni and P.

HRTEM was performed to gain further information about the microstructure (Figure 25c), and the measured interplanar distance of the crystallite is ca. 0.21 nm, which corresponds to the lattice spacing of (111) crystal planes of hexagonal CoNiP (ICDD No. 04-001-4562), consistent with the XRD result (Figure 24a). High-angle annular dark-field STEM (HAADF-STEM) was carried out to investigate the elemental distribution of the CoNiP NPs. As shown in Figure 25d, the elements Co, Ni and P are uniformly distributed over the CoNiP NPs.

4.1.2 Surface chemical states

XPS analysis was performed to investigate the surface chemical states of the as-obtained CoNiP NPs (Figure 26). Similar to the TEM result, the XPS measurements confirmed the presence of the corresponding elements in the as-synthesized CoNiP catalysts. It should be noted that the carbon signal in Figure 26a arises from the carbon adhesive tape used in XPS measurement or/and environmental pollution. The oxygen signal should originate from the surface oxidation of samples in air, which will be illustrated in the following.

Figure 26b shows the high-resolution Co $2p_{3/2}$ XPS spectrum. Peak deconvolution shows two main peaks at 778.7 and 781.8 eV and one satellite peaks at 786.3 eV. The characteristic binding energy (BE) peak at

778.7 eV generally relates to the Co 2p contribution of cobalt-nickel phosphides, which is a good indication of Co–Ni–P bond formation; while the BE peak at 781.8 eV may be associated with the oxidized Co species (phosphates) that likely result from the slight surface oxidation. Similar peak deconvolution in the Ni 2p spectra was displayed in Figure 26c, showing that there are two main peaks at 853.4 and 856.4 eV and one satellite peaks at 862 eV. The BE peak at 853.4 eV relates to the Ni 2p contribution of cobalt-nickel phosphides; while the BE peak at 856.4 eV may be associated with the oxidized Ni species (phosphates) that perhaps stem from surface oxidation. As far as the P 2p spectra (Figure 26d) is concerned, two BE peaks appear at 129.5 and 130.8 eV, which can be assigned to the low-valence phosphorus and the $2p_{3/2}$ and $2p_{1/2}$ core levels of central phosphorus atoms in the phosphide, respectively, further confirming the formation of Co–Ni–P bonds in the phosphide. Corresponding to the peaks at 781.8 eV in Co 2p spectrum and 856.4 eV Ni 2p spectrum, there is one peak located at 133.8 eV in P 2p spectrum, which can be assigned to the P–O bonding in the phosphates from the surface oxidation upon exposing the samples to air.
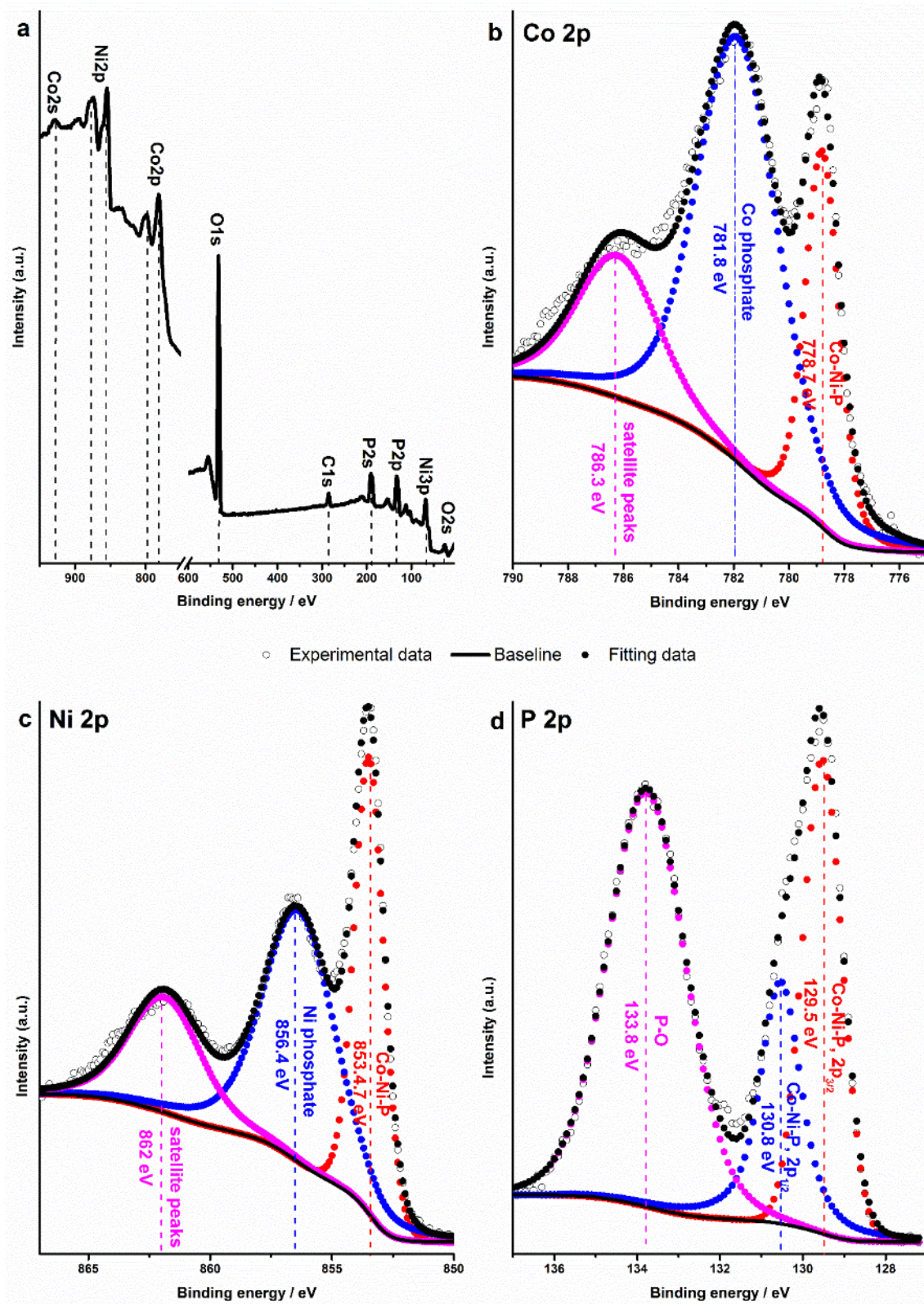
Figure 26. XPS (a) survey spectrum, (b) Co 2p, (c) Ni 2p and (d) P 2p spectra of the CoNiP NP catalysts.

4.1.3 OER performance of the CoNiP NPs

The OER performance of the CoNiP NPs was investigated in 1.0 M KOH electrolyte using CV. The electrocatalytic performance of the commercial RuO_2 was also measured under the same conditions for the comparison. The catalysts were loaded on CP substrates with a loading density of 0.3 mg cm^{-2}. Prior to the catalytic test, pre-activation was carried out by repetitive CV scans at 5 mV s^{-1} in the potential range of 1.44 to 1.63 V vs RHE until a steady state CV curve was obtained. Figure 27 a shows the cathodic branches of iR-corrected CV curves of all samples after pre-activation.
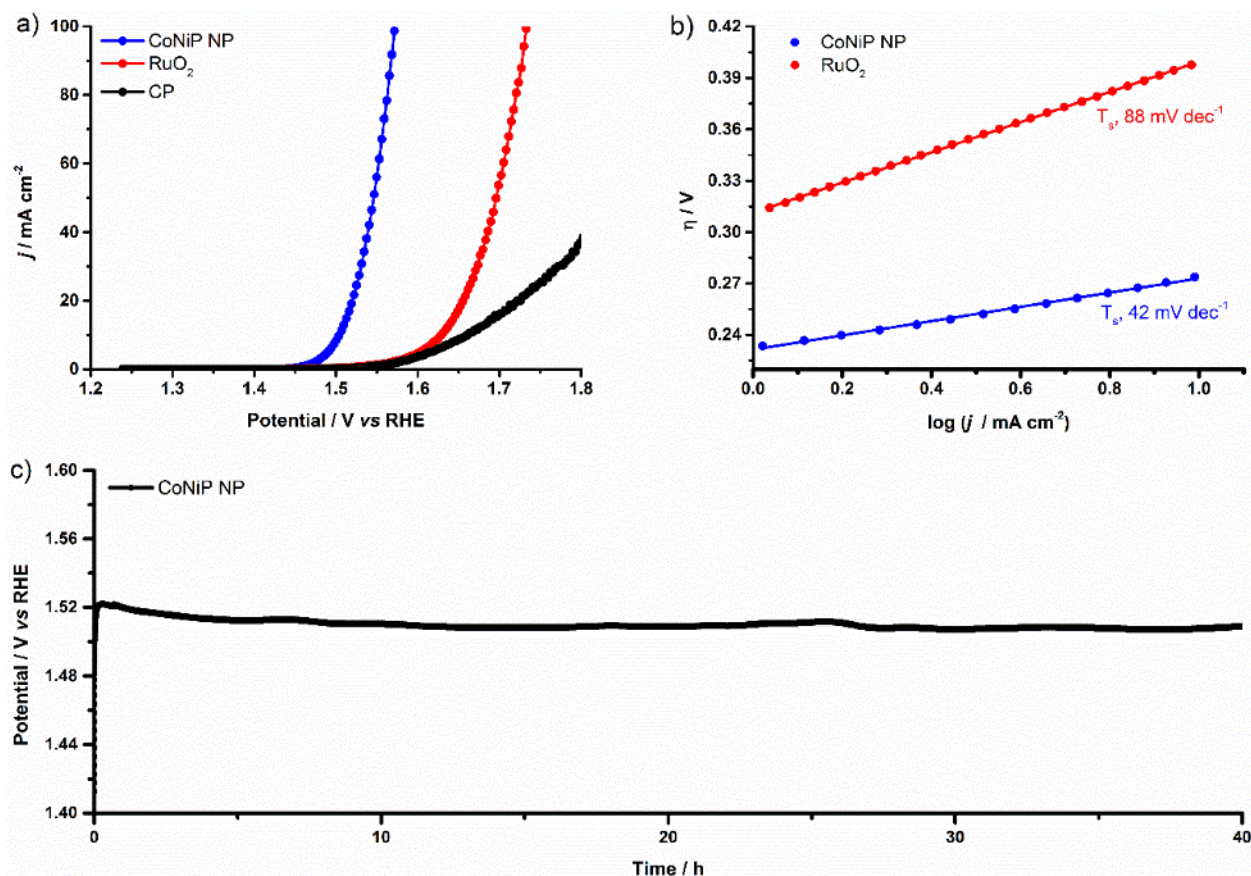
Figure 27. OER performance of CoNiP catalysts measured in 1.0 M KOH electrolyte with a catalyst loading density of 0.3 mg cm^{-2}. The OER performances of commercial RuO_2 and CP substrate is given for comparison. (a) iR-corrected polarization curves recorded at a scan rate of 5 mV s^{-1}. (b) Tafel plots. (c) Stability test recorded at a constant current density of 10 mA cm^{-2} at room temperature.

The bare CP substrate only generates negligible current density, suggesting that it's not catalytically active towards the OER. The overpotential (η_{10}) needed to deliver the benchmark current density of 10 mA cm^{-2} is

broadly used as an indicator to compare the catalytic activity. The CoNiP NPs only need a η_{10} of 260 mV to deliver 10 mA cm^{-2}, substantially lower than that of commercial RuO$_2$ NPs (η_{10} = 400 mV).

The OER kinetics of all catalysts was investigated by the Tafel analysis. As shown in Figure 27b, the Tafel slope of CoNiP NPs is only 42 mV dec^{-1}, smaller than that of the commercial RuO$_2$ (88 mV dec^{-1}), suggesting a more favorable OER rate at the CoNiP NPs.

The catalytic stability as a crucial performance indicator was assessed using GE at a constant current density of 10 mA cm^{-2} (Figure 27c). The CoNiP NPs showed very good stability, and could sustain at 10 mA cm^{-2} with little degradation for at least 40 h.

4.1.4 HER performance of the CoNiP NPs

The electrocatalytic performance of the CoNiP NPs towards the HER was also assessed on CP substrates under both acid and alkaline conditions using CV with a loading density of 0.3 mg cm^{-2}. As shown in Figures 28a and 28b, the CP supports do not show notable cathodic current in both acid and alkaline conditions, indicating that they are catalytically inactive for the HER. Commercially available Pt/C as the state-of-the-art HER catalysts, was also assessed as a benchmark under the same conditions, which shows the best HER activities in both acidic and alkaline solutions (Figures 28a and 28b). In acid electrolyte, the Pt/C catalyst only requires a small η_{10} of 40 mV to deliver 10 mA cm^{-2}, while the CoNiP NP catalysts exhibit comparatively large η_{10} values of 140 mV to reach the same current density. In alkaline electrolyte, the Pt/C catalyst also exhibits excellent HER performance, only requiring η_{10} of 37 mV to deliver 10 mA cm^{-2}, while the CoNiP NP catalysts demand a η_{10} value of 130 mV to deliver the same current density. The HER kinetics of all catalysts was investigated by the Tafel analysis. As shown in Figures 28c and 28d, the Tafel slopes of CoNiP NPs are 175 and 104 mV dec^{-1} in acid and alkaline solution, respectively, lower than those of the Pt/C (42 vs 50 mV dec^{-1}), consist with the performance test. The catalytic stability of the CoNiP NPs catalysts was evaluated by CP at a constant current density of -10 mA cm^{-2} in both 0.5 M H$_2$SO$_4$ and 1.0 M KOH. As shown in Figures 28e and 28f, the CoNiP NPs show very good stability in both acidic and alkaline media in the course of 40 h GE, with little degradation.
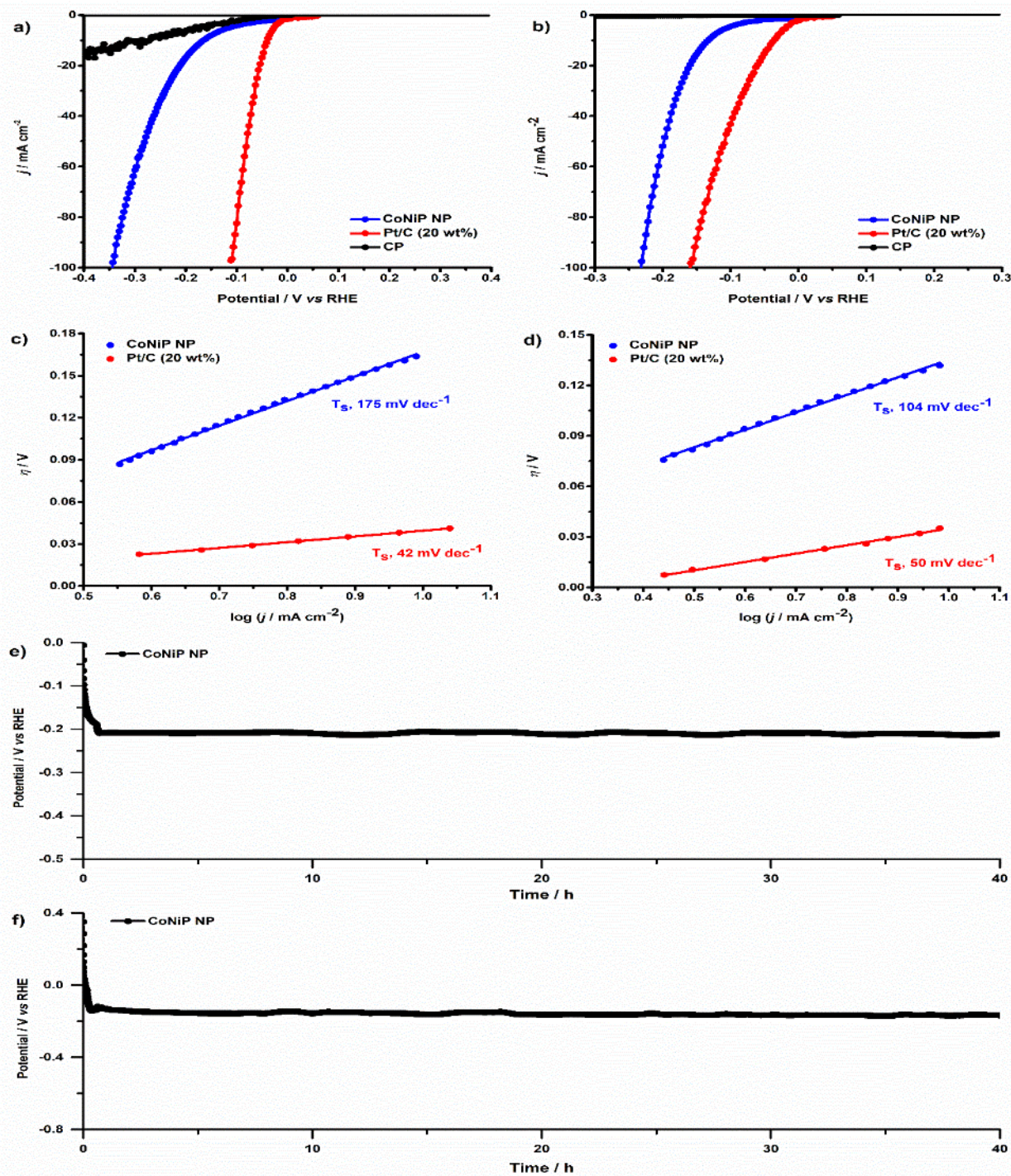
Figure 28. HER performance of CoNiP NP catalysts measured at room temperature. The HER performances of commercial Pt/C (20 wt%) and CP substrate is given for comparison. *iR*-corrected polarization curves recorded in (a) 0.5 M H_2SO_4 and (b) 1.0 M KOH. Scan rate: 5 mV s^{-1}. Comparison of the Tafel slopes of CoNiP NP catalysts and Pt/C (20 wt%) measured in (c) 0.5 M H_2SO_4 and (d) 1.0 M KOH. Stability test of CoNiP NP catalysts recorded at a constant current density of -10 mA cm^{-2} in (e) 0.5 M H_2SO_4 and (f) 1.0 M KOH.

4.1.5 OWE electrocatalytic performance

Given the above excellent catalytic performance in alkaline media, an electrolyzer was assembled using CP-supported CoNiP NPs as both anode and cathode, and OWE was carried out in 1.0 M KOH solution. For comparison, a control electrolyzer comprising RuO_2 (anode) and Pt/C 20wt% (cathode) noble-metal catalysts supported on CP (RuO_2||Pt/C) was also fabricated.
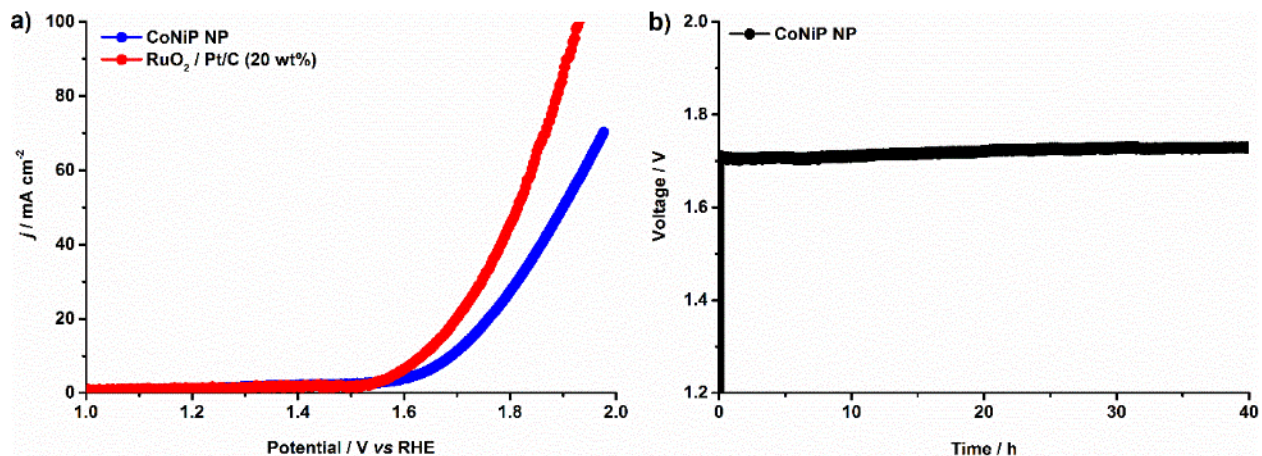
Figure 29. OWE performance of prototype electrolyzers measured in a two-electrode configuration in 1.0 M KOH. (a) Polarization curves of CoNiP NP electrolyzers and RuO_2(+)||20wt% Pt/C(-) recorded at a scan rate of 5 mV s^{-1} without *iR*-correction. (b) Stability test of the CoNiP NP electrolyzer recorded at a constant current density of 10 mA cm^{-2} without *iR*-correction.

Figure 29a shows the polarization curves of the CoNiP NP and RuO_2||Pt/C electrolyzers measured in a two-electrode configuration. The CoNiP NP electrolyzer only requires cell voltages of 1.7 V (V_{10}) to deliver a current density of 10 mA cm^{-2}. This voltage is only slightly larger than that of the noble metal based RuO_2||Pt/C (V_{10} = 1.63 V), showing substantial promise for use as inexpensive catalysts for water splitting . Long-term electrocatalytic stability of the CoNiP NPs electrolyzer was evaluated by galvanostatic water splitting at 10 mA cm^{-2} (Figure 29b). Impressively, the electrolyzer was able to operate at 10 mA cm^{-2} over 40 h with negligible degradation.

4.2   Porous CoP foam for water splitting

4.2.1 Performance optimization of the porous CoP foam
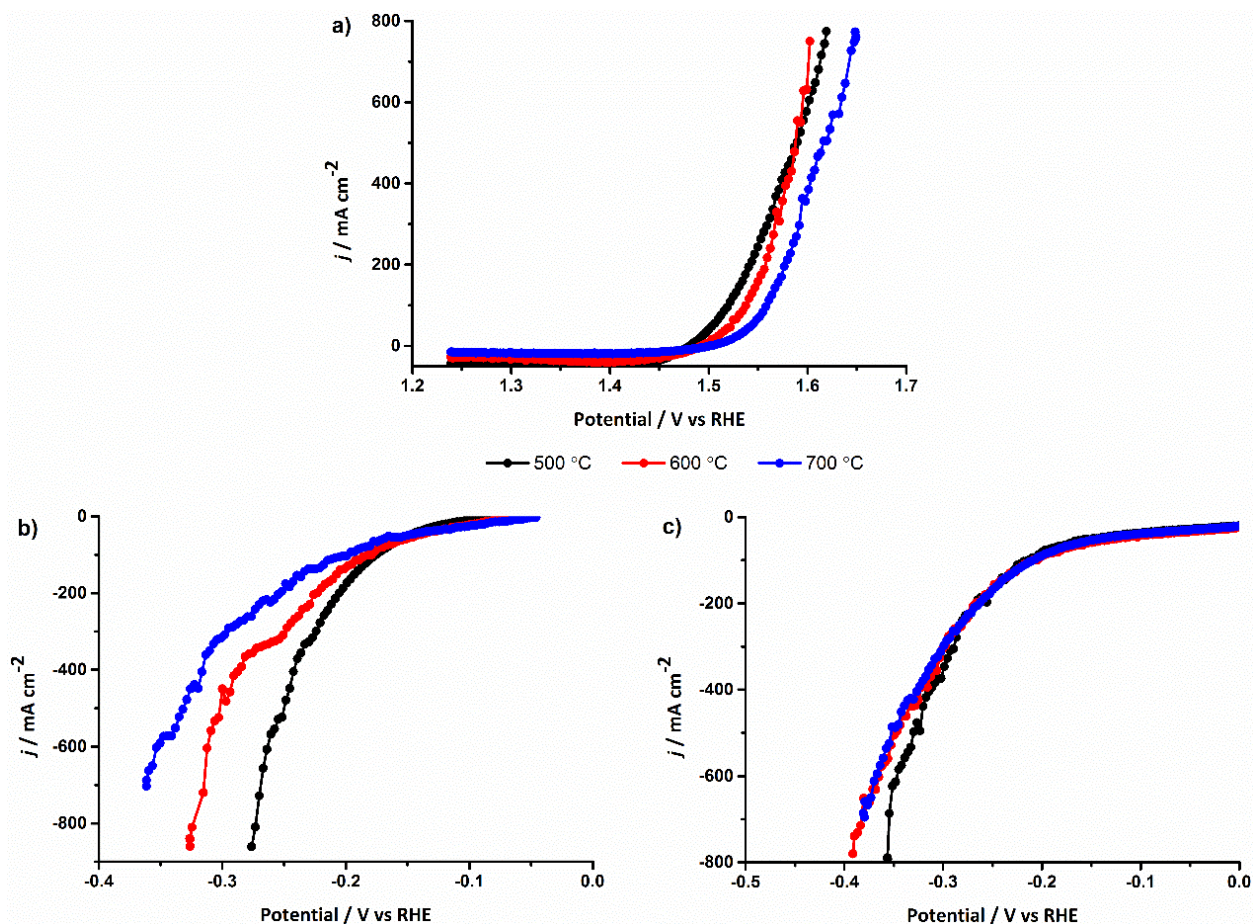
Figure 30. Performance optimization of porous cobalt phosphide foam electrodes. The *iR*-corrected polarization curves recorded at a scan rate of 5 mV s^{-1} at room temperature for (a) OER in 1.0 M KOH, (b) HER in 0.5 M H$_2$SO$_4$ and (c) HER in 1.0 M KOH.

In order to maximize the performance of the obtained porous CoP foam electrodes, the OER and HER performance of the samples prepared at different phosphorization temperatures (500, 600 and 700 °C) is investigated, and the results are summarized in Figure 30. It can be clearly seen that the samples phosphorized at 500 °C deliver the best OER (alkaline) and HER (both alkaline and acid) performance, and thus 500 °C was used for the synthesis of the porous CoP foam.

4.2.2 Morphology and nanostructure of porous CoP foam

The crystalline structure of as-prepared porous CoP foam was firstly examined by XRD, and the pristine CF was also tested as a reference.
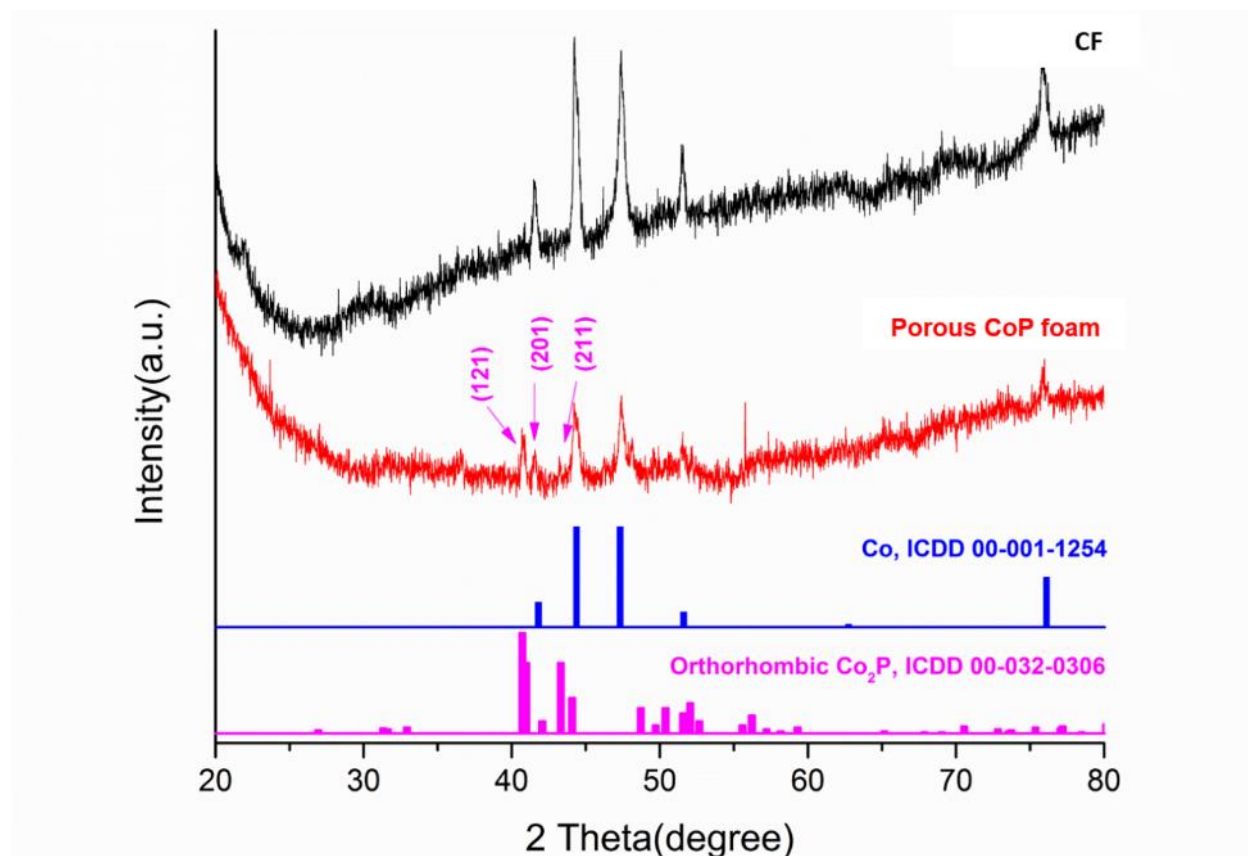
Figure 31. XRD patterns of pristine CF and porous CoP foam.

As shown in Figure 31, after phosphorization, apart from the five diffraction peaks of pristine CF, three weak diffraction peaks at 40.8°, 41.6° and 43.2° appear, corresponding to the (121), (201) and (211) lattice planes of orthorhombic Co_2P phase (ICDD No. 00-032-0306), which verifies the formation of Co_2P on CF.
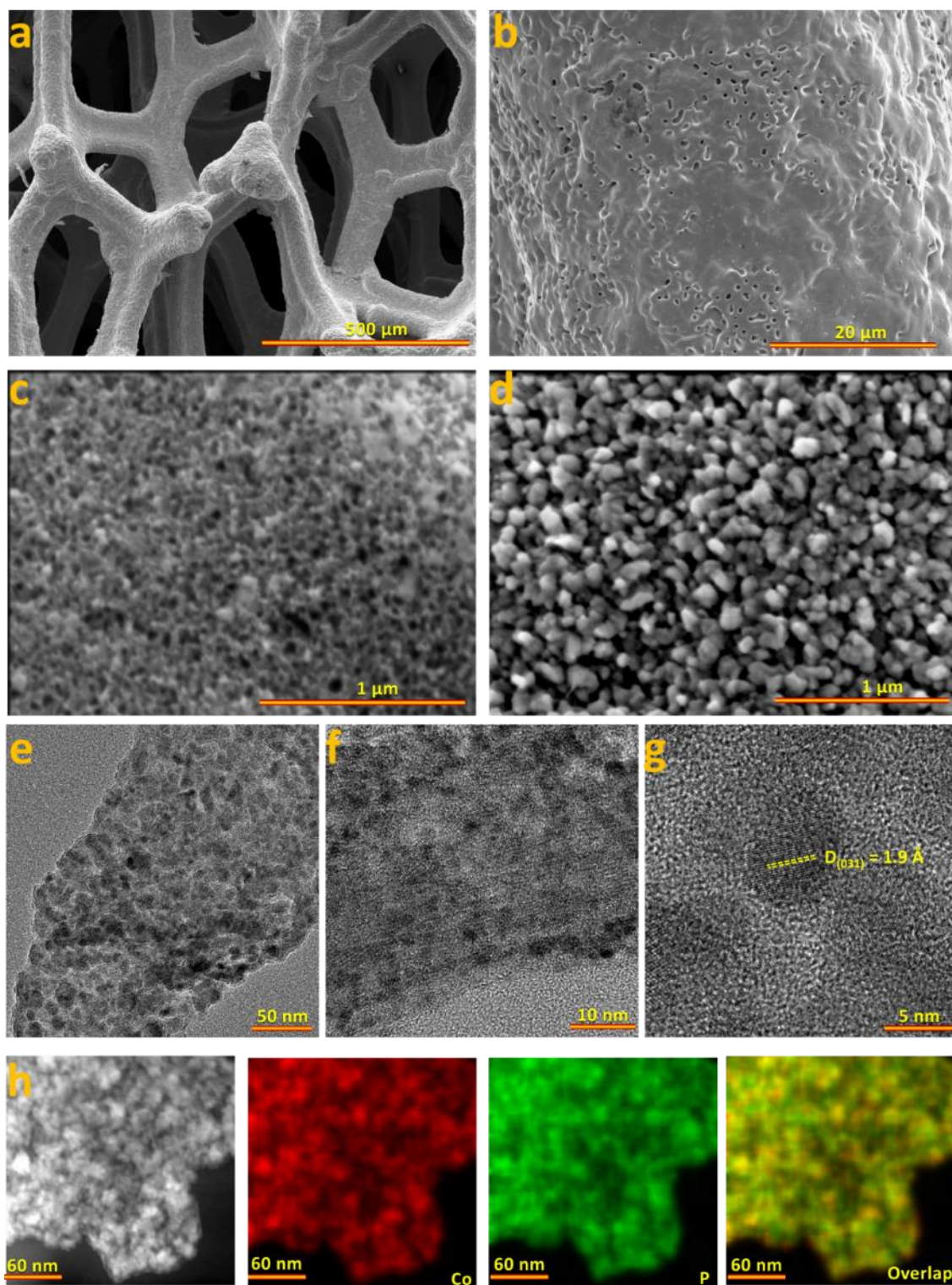
Figure 32. SEM of (a,b) pristine CF, (c) CF after anodization and thermal annealing, (d) porous CoP foam. (e, f) TEM images taken at different magnifications, (g) HRTEM, (h) HAADF image and elemental maps of Co, P and their overlap of porous CoP foam.

The morphology of the pristine CF and CF after anodization, thermal annealing and phosphorization was examined by electron microscopy. As shown in Figures 32a and 32b, the pristine CF is composed of interconnected Co ligaments with smooth surface. After anodization and thermal annealing treatment, the morphology has been altered dramatically, where one can see that the original smooth surface has disappeared and a well-defined porous structure has been obtained (Figure 32c). The porous structure was replaced by a high density of nanoparticles after phosphorization (Figure 32d). This could be attributed to the strong phosphorization effect of red phosphorus at high temperature of 500 °C. To gain more structure information in the as-synthesized porous CoP foam, the TEM was further performed (Figures 32e-32h). Low- and high-magnification TEM observation (Figures 32e and 32f) revealed that the formed big particles shown in SEM (Figure 32d) are composed of many crystalline grains with the NP size of ca. 3-5 nm. A HRTEM image is illustrated in Figure 32g, where the lattice fringes of crystal grains can be clearly resolved. The measured interplanar distance of the crystallite is ca. 0.19 nm, which corresponds to the lattice spacing of (031) crystal planes of orthorhombic Co_2P (ICDD No. 00-032-0306). HAADF-STEM was further carried out to investigate the elemental distribution of the CoP. As shown in Figure 32h, the elements Co and P are uniformly distributed over the CoP.

4.2.3 Surface chemical states of porous CoP foam

The surface chemical states of the as-obtained porous CoP foam were investigated by XPS characterization (Figure 33). Similar to the XPS survey spectrum of CoNiP NPs (Figure 26), the carbon signal in Figure 33a should come from adventitious carbon. The high-resolution Co $2p_{3/2}$ XPS spectrum is shown in Figure 33b, and it can be seen that two main peaks appear at 778.9 and 781.3 eV after peak deconvolution. The characteristic binding energy (BE) peak at 778.9 eV can be ascribed to the Co 2p contribution of cobalt phosphide, which proves that the Co–P bond has formed; while the BE peak at 781.3 eV may be associated with the oxidized Co species (phosphates) arising from surface oxidation in air. As for the P 2p spectrum (Figure 33c), two BE peaks appear at 129.7 and 130.6 eV in the low BE range of P spectrum, corresponding to the $2p_{3/2}$ and $2p_{1/2}$ core levels of central phosphorus atoms in the phosphide, respectively. This further corroborates the formation of Co–P bonds in the phosphide. Similarly, there is one peak located at 134.2 eV in P XPS spectrum, which should originate from the P–O bonding in the phosphates due to surface oxidation upon exposing the samples to air.
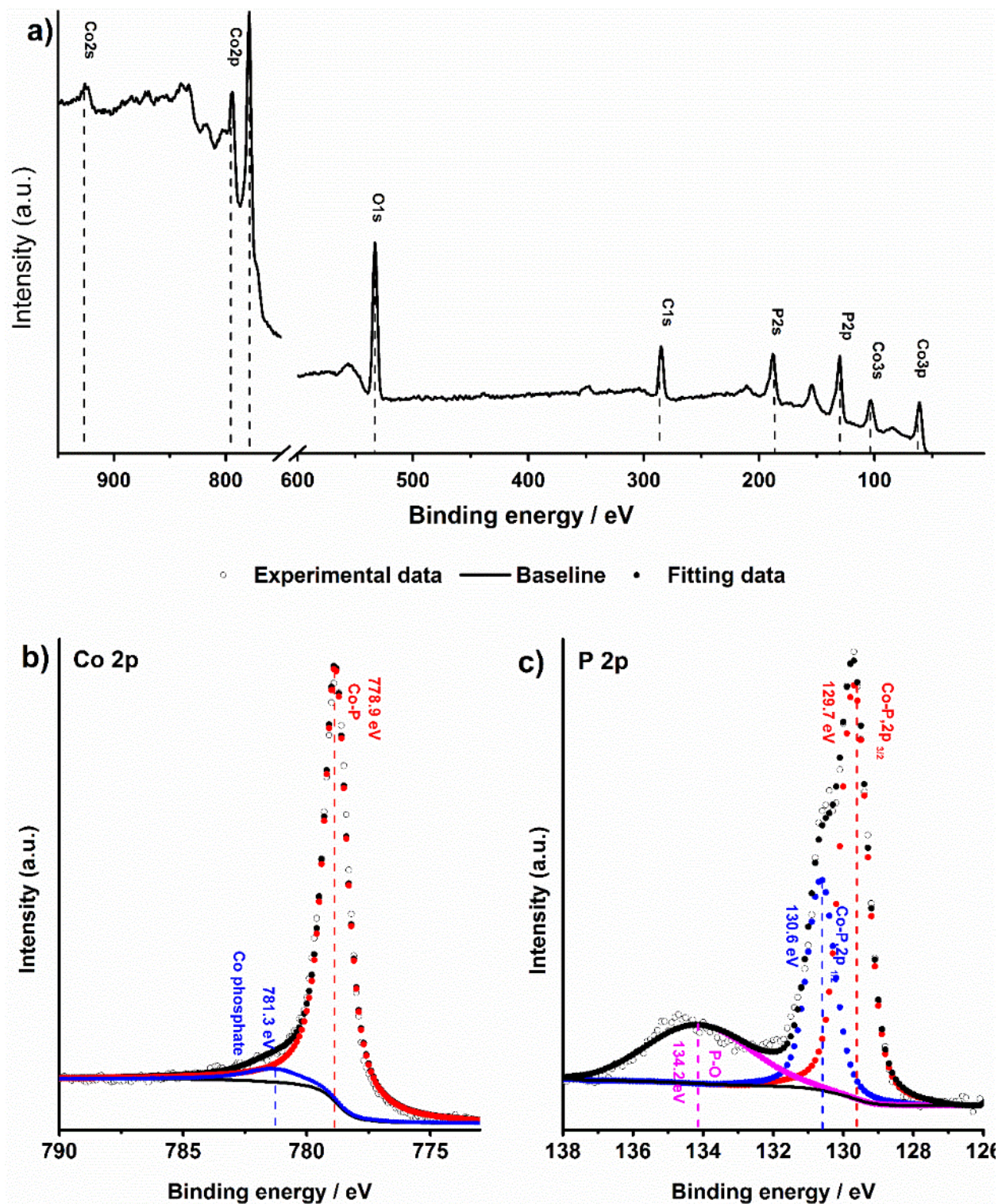
Figure 33. . XPS characterization of the porous CoP foam. (a) Survey spectrum, (b) Co 2p and (c) P 2p high-resolution XPS spectra.

4.2.4 OER and HER performance of the porous CoP foam

The OER performance of the porous CoP foam was investigated in 1.0 M KOH electrolyte using CV. The electrocatalytic performance of pristine CF substrate was also measured under the same conditions for comparison. Prior to each catalytic test, pre-activation was carried out by repetitive CV scans at 5 mV s^{-1} in the potential range of 1.2 – 1.7 V *vs.* RHE until a steady state CV curve was obtained, and the polarization curves of the reduction branch was considered for performance comparison. As shown in Figure 34a, although the bare CF shows catalytic activity towards OER, it is dramatically lower than that of porous CoP foam. For example, the overpotential needed to deliver 1000 mA cm^{-2} is only 380 mV for porous CoP foam, which is ca. 70 mV lower than that of pristine CF.

Figure 34. OER and HER performances of porous CoP foam electrodes measured in 1.0 M KOH electrolyte. The OER performances of CF substrate is given for comparison. (a) *iR*-corrected OER polarization curves recorded at a scan rate of 5 mV s^{-1}. (b) *iR*-corrected HER polarization curves recorded at a scan rate of 5 mV s^{-1}. (c) Stability test of porous CoP foam recorded at a constant current density of 500 (OER) and -500 (HER) mA cm^{-2} at room temperature.

The HER performance of the porous CoP foam was also investigated in 1.0 M KOH electrolyte using CV. As shown in Figure 34b, the bare CF doesn't generate appreciable current densities until -0.4 V vs RHE, showing that it is inert towards HER. In comparison, much higher HER performance was obtained in the porous CoP foam, and the overpotential needed to afford -1000 mA cm^{-2} is merely 290 mV. This superior performance indicates that the phosphorization treatment and the porous structure indeed substantially improve both OER and HER performance.

Furthermore, the catalytic stability as a crucial performance indicator was assessed using GE at a constant current density of 500 (OER) and -500 (HER) mA cm^{-2} (Figure 34c). The porous CoP foam showed very good stability for OER and HER, and could sustain at high current densities of 500 and -500 mA cm^{-2} with no degradation for at least 500 h.

4.2.5 OWE electrocatalytic performance

Given the excellent catalytic performance of porous CoP foam in alkaline media, an electrolyzer was assembled using two pieces of porous CoP foam as the anode and cathode, respectively, and the OWE performance of the CF substrate was also measured under the same conditions for comparison. Figure 35a shows the polarization curves of the porous CoP foam and CF electrolyzers measured in a two-electrode configuration without iR-correction.

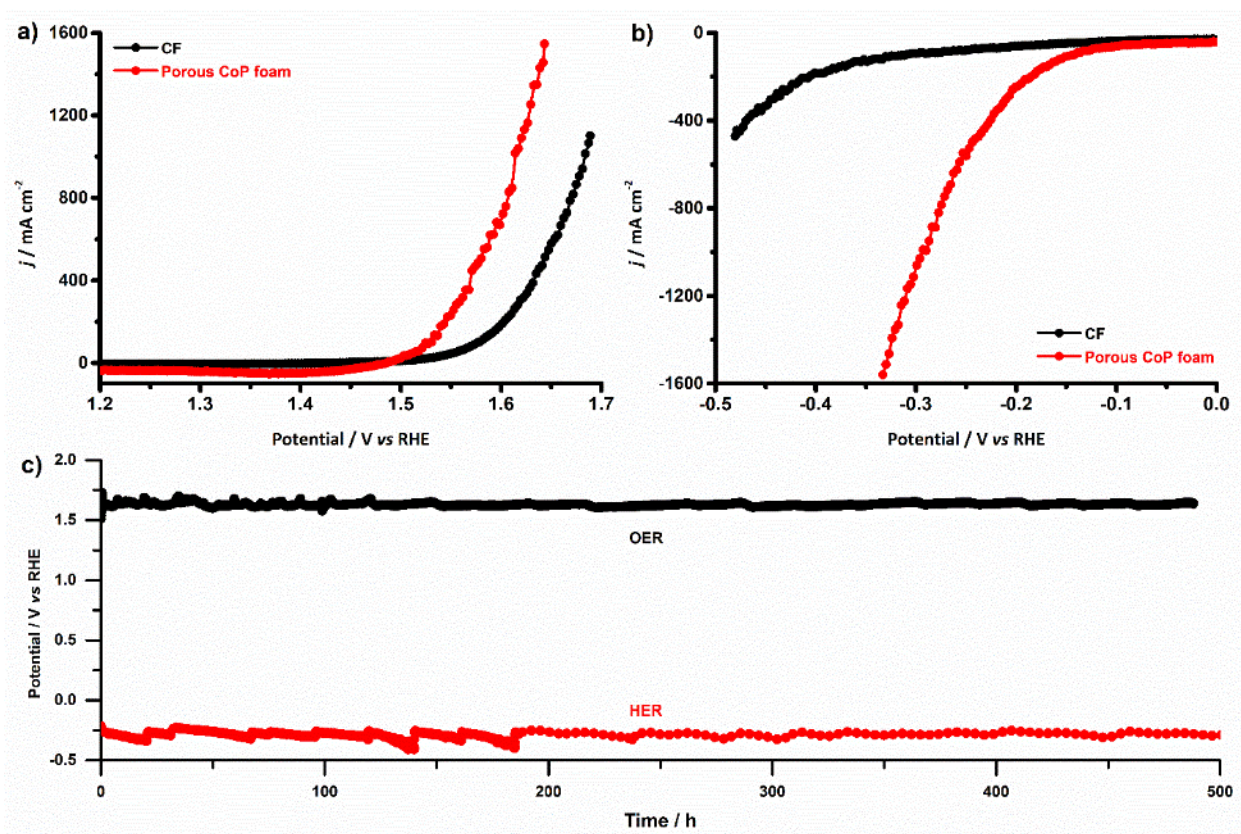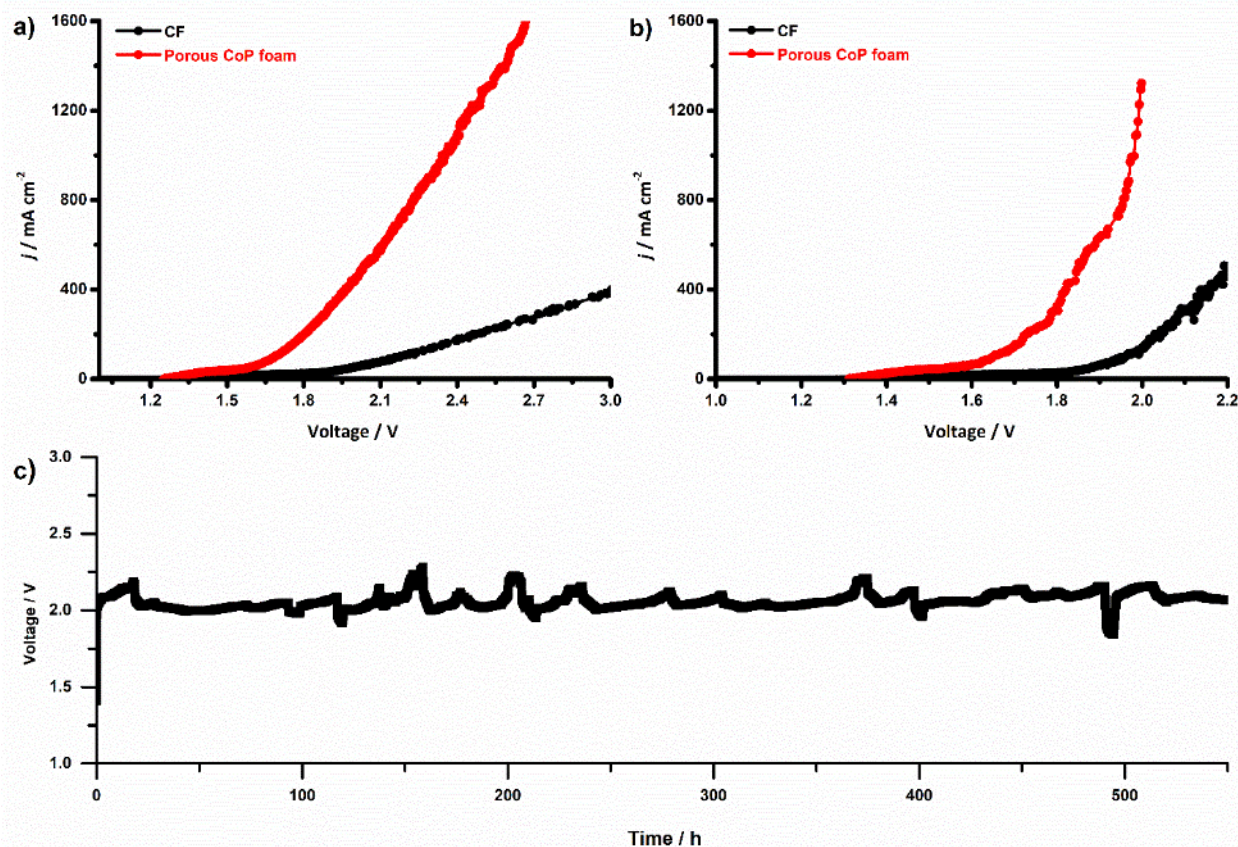Figure 35. OWE performance of porous CoP foam measured in 1.0 M KOH electrolyte. The performance of CF substrate is given for comparison. Polarization curves recorded at a scan rate of 5 mV s^{-1} without (a) and with (b) iR-correction. (c) Stability test of porous CoP foam recorded at a constant current density of 500 mA cm^{-2} at room temperature without iR-correction.

The porous CoP foam electrolyzer significantly outperforms the CF electrolyzer, due to the outstanding OER and HER performance of the porous CoP foam. For example, to deliver a high and industrially relevant currdent density of 1000 mA cm^{-2}, the CoP foam electrolyzer only needs a voltage of 2.35 V (Figure 35a), which will be further reduced to 1.98 V after the iR- correction (Figure 35b). In contrast, the CF electrolyzer only generates a currdent density of 115 mA cm^{-2} at the same voltage of 1.98 V (Figure 35b). The superior OWE performance further proves that phosphorization and porous structure indeed substantially boost electrocatalytic performance. Furthermore, the porous CoP foam electrolyzer was able to operate at 500 mA cm^{-2} over 500 h with negligible degradation.

Chapter 5. Conclusions

This chapter summarizes the major conclusions of this work.

This thesis focuses on the design and synthesis of cobalt-based transition metal phosphide nanostructures for use as efficient and durable catalysts for the HER (acid and alkaline media) and the OER (alkaline media) of water splitting. Two types of electrocatalysts have been investigated: the first one is powdery cobalt nickel phosphide nanoparticles (CoNiP NPs) with high intrinsic activity per active site; the second one is self-supported porous CoP foam with a large number of active sites in a given geometric area. Both catalysts were comprehensively characterized using a wide spectrum of techniques and their electrocatalytic performance thoroughly investigated.

The doped powdery CoNiP NPs catalyst was synthesized by wet chemical reduction of transition metal precursors, followed by subsequent gas-solid phosphorization. Doping of nickel atoms into cobalt phosphide is expected to increase the intrinsic catalytic activity of the catalyst by increasing the catalytic performance of each active site. XRD examination showed that CoNiP NPs consist exclusively of hexagonal phase CoNiP mixed phosphide. The morphology, microstructure and composition of CoNiP NPs were further examined by TEM characterization. TEM observation revealed that CoNiP NPs are aggregated with a narrow particle size distribution (5-10 nm). HRTEM confirmed the high degree of crystallinity of CoNiP, consistent with the XRD results. XPS analysis verified the presence of Co, Ni, and P elements in the as-synthesized CoNiP catalysts. The CoNiP NPs showed good electrocatalytic activities toward the OER in alkaline media and the HER in both alkaline and acid media, as well as outstanding long-term operational stability. Under OER conditions, the CoNiP NPs only need 260 mV to deliver 10 mA cm^{-2}, and their Tafel slope is only 42 mV dec^{-1}. Moreover, CoNiP NPs can sustain at 10 mA cm^{-2} with little degradation for at least 40 h. Under HER conditions, the CoNiP NP catalysts exhibited comparatively high overpotentials of 140 and 130 mV to deliver 10 mA cm^{-2}, in acid electrolyte and alkaline electrolyte, respectively. The Tafel slopes of CoNiP NP catalysts for HER are 175 and 104 mV dec^{-1}, respectively, in acid and alkaline solutions. Moreover, the CoNiP NPs showed very good HER stability in both acidic and alkaline media in the course of 40 h GE, with only little degradation. An electrolyzer was assembled and tested for overall water splitting in 1.0 M KOH solution. The CoNiP NP electrolyzer only requires a cell voltage of 1.7 V to deliver a current density of 10 mA cm^{-2} and shows the good long-term electrocatalytic stability, operating at 10 mA cm^{-2} over 40 h with negligible degradation.

Self-supported porous CoP foam was obtained successfully using low-temperature electrochemical anodization, thermal annealing in air and phosphorization treatment using red phosphorus as the phosphorus source. The unique structure of self-supported porous CoP foam is expected to increase the

catalytic performance by increasing the number of active sites and facilitating mass transfer during the reaction. Upon optimization, it was found that the samples phosphorized at 500 °C showed the best OER and HER properties. Such porous CoP foam electrode is highly porous and consists of orthorhombic Co_2P phase, as revealed by SEM and XRD characterization. TEM observation confirmed that the obtained big particles are composed of many small crystallites with a size of ca. 3-5 nm. Moreover, these crystallites have a high degree of crystallization, as verified by HRTEM. HAADF-STEM proved that the Co and P elements are uniformly distributed over the CoP foam. XPS analysis confirmed the presence of Co and P in the as-prepared porous CoP foam. The porous CoP exhibited excellent catalytic activities towards the OER and HER in alkaline media. The overpotentials needed to deliver 1000 mA cm^{-2} are 380 and 290 mV for OER and HER, respectively. Moreover, the porous CoP foam also showed very good stability for OER and HER, and could sustain at high current densities of 500 and -500 mA cm^{-2} with little degradation for at least 500 h. The porous CoP foam electrolyzer exhibited outstanding OWE performance, demanding a comparatively low voltage of 2.35 V to deliver a high current density of 1000 mA cm^{-2}. Furthermore, the porous CoP foam was able to operate at 500 mA cm^{-2} over 500 h with negligible degradation.

In summary, cobalt-based water splitting catalysts with both excellent activity and operational stability have been developed in this work. The research provides new insight in improving the water splitting performance of metal phosphide catalysts by rational design. The experiment results demonstrate that doping and microstructural engineering are effective approaches to increasing electrocatalytic activity of a catalyst. Meanwhile, the work offers useful guidelines for the synthesis of this specific class of earth-abundant water splitting catalysts. The synthetic strategy reported here can be readily extended to prepare other electrocatalysts. For example, bi-metallic or tri-metallic phosphide nanostructures could also be synthesized in the form of powders or self-supported foam using the methods reported in this thesis.

Chapter 6. References

Acar, C., & Dincer, I. (2014). Comparative assessment of hydrogen production methods from renewable and non-renewable sources. *International Journal of Hydrogen Energy*, *39*(1), 1–12. https://doi.org/10.1016/j.ijhydene.2013.10.060

Anderson, D. L. (1983). Chemical composition of the mantle. *Journal of Geophysical Research*, *88*(S01), B41. https://doi.org/10.1029/JB088iS01p00B41

Baykara, S. Z. (2018). Hydrogen: A brief overview on its sources, production and environmental impact. *International Journal of Hydrogen Energy*, *43*(23), 10605–10614. https://doi.org/10.1016/j.ijhydene.2018.02.022

Belz, S. (2016). A synergetic use of hydrogen and fuel cells in human spaceflight power systems. *Acta Astronautica*, *121*, 323–331. https://doi.org/10.1016/j.actaastro.2015.05.031

Benck, J. D., Hellstern, T. R., Kibsgaard, J., Chakthranont, P., & Jaramillo, T. F. (2014). Catalyzing the Hydrogen Evolution Reaction (HER) with Molybdenum Sulfide Nanomaterials. *ACS Catalysis*, *4*(11), 3957–3971. https://doi.org/10.1021/cs500923c

Bockris, J. O'M., Conway, B. E., Yeager, E., & White, R. E. (1981). *Comprehensive Treatise of Electrochemistry*. (J. O'M. Bockris, B. E. Conway, E. Yeager, & R. E. White, Eds.) (1st ed., Vol. 4). Boston, MA: Springer US. https://doi.org/10.1007/978-1-4684-3785-0

Bockris, John O'M., Reddy, A. K. N., & Maria E. Gamboa-Aldeco. (2000). *Modern Electrochemistry 2A Fundamentals of Electrodics* (2nd ed.). New York: Springer US. https://doi.org/10.1007/b113922

Burstein, G. T. (2005). A hundred years of Tafel's Equation: 1905–2005. *Corrosion Science*, *47*(12), 2858–2870. https://doi.org/10.1016/j.corsci.2005.07.002

Cabán-Acevedo, M., Stone, M. L., Schmidt, J. R., Thomas, J. G., Ding, Q., Chang, H.-C., … Jin, S. (2015). Efficient hydrogen evolution catalysis using ternary pyrite-type cobalt phosphosulphide. *Nature Materials*, *14*, 1245. Retrieved from https://doi.org/10.1038/nmat4410

Callejas, J. F., McEnaney, J. M., Read, C. G., Crompton, J. C., Biacchi, A. J., Popczun, E. J., … Schaak, R. E. (2014). Electrocatalytic and Photocatalytic Hydrogen Production from Acidic and Neutral-pH Aqueous Solutions Using Iron Phosphide Nanoparticles. *ACS Nano*, *8*(11), 11101–11107. https://doi.org/10.1021/nn5048553

Chatterjee, A. K. (2001). X-Ray Diffraction. In Ramachandran, V.S. & James J. Beaudoin (Eds.), *Handbook of Analytical Techniques in Concrete Science and Technology* (1st ed., pp. 275–332). William Andrew Publishing. https://doi.org/10.1016/B978-081551437-4.50011-4

Chen, M., Qi, J., Zhang, W., & Cao, R. (2017). Electrosynthesis of NiPx nanospheres for electrocatalytic hydrogen evolution from a neutral aqueous solution. *Chem. Commun.*, *53*(40), 5507–5510. https://doi.org/10.1039/C7CC01584D

Cherevko, S., Geiger, S., Kasian, O., Kulyk, N., Grote, J. P., Savan, A., ... Mayrhofer, K. J. J. (2016). Oxygen and hydrogen evolution reactions on Ru, RuO2, Ir, and IrO2 thin film electrodes in acidic and alkaline electrolytes: A comparative study on activity and stability. *Catalysis Today*, *262*, 170–180. https://doi.org/10.1016/j.cattod.2015.08.014

David Harvey. (2000). *Modren analytical chemistry* (1st ed.). US: McGraw-Hill Higher Education.

Eatwell-Hall, R. E. A., Sharifi, V. N., & Swithenbank, J. (2010). Hydrogen production from molten metal gasification. *International Journal of Hydrogen Energy*, *35*(24), 13168–13178. https://doi.org/10.1016/j.ijhydene.2010.09.003

Elreedy, A., & Tawfik, A. (2015). Effect of Hydraulic Retention Time on Hydrogen Production from the Dark Fermentation of Petrochemical Effluents Contaminated with Ethylene Glycol. *Energy Procedia*, *74*, 1071–1078. https://doi.org/10.1016/j.egypro.2015.07.746

Evans, A., Strezov, V., & Evans, T. J. (2009). Assessment of sustainability indicators for renewable energy technologies. *Renewable and Sustainable Energy Reviews*, *13*(5), 1082–1088. https://doi.org/10.1016/j.rser.2008.03.008

Han, A., Zhang, H., Yuan, R., Ji, H., & Du, P. (2017). Crystalline Copper Phosphide Nanosheets as an Efficient Janus Catalyst for Overall Water Splitting. *ACS Applied Materials & Interfaces*, *9*(3), 2240–2248. https://doi.org/10.1021/acsami.6b10983

Heng, L., Zhang, H., & Xiao, R. (2016). Hydrogen production from heavy fraction of bio-oil using iron-based chemical looping process : Thermodynamic simulation and performance analysis. *International Journal of Hydrogen Energy*, *41*(40), 17771–17783. https://doi.org/10.1016/j.ijhydene.2016.07.068

Hofmannz, H. (1998). ELECTROLYSIS : THE IMPORTANT ENERGY TRANSFORMER. *International Association for Hydrogen Energy*, *23*(8).

Huang, Z., Chen, Z., Chen, Z., Lv, C., Meng, H., & Zhang, C. (2014). Ni12P5 Nanoparticles as an Efficient Catalyst for Hydrogen Generation via Electrolysis and Photoelectrolysis. *ACS Nano*, *8*(8), 8121–8129. https://doi.org/10.1021/nn5022204

International Energy Agency. (2019). *Global Energy & CO2 Status Report 2018*. *INTERNATIONAL ENERGY AGENCY*.

Jiang, P., Liu, Q., Liang, Y., Tian, J., Asiri, A. M., & Sun, X. (2014). A Cost-Effective 3D Hydrogen Evolution Cathode with High Catalytic Activity: FeP Nanowire Array as the Active Phase. *Angewandte Chemie International Edition*, *53*(47), 12855–12859. https://doi.org/10.1002/anie.201406848

Jiang, P., Liu, Q., & Sun, X. (2014). NiP2 nanosheet arrays supported on carbon cloth: an efficient 3D hydrogen evolution cathode in both acidic and alkaline solutions. *Nanoscale*, *6*(22), 13440–13445. https://doi.org/10.1039/C4NR04866K

Jiao, Y., Zheng, Y., Jaroniec, M., & Qiao, S. Z. (2015). Design of electrocatalysts for oxygen- and hydrogen-involving energy conversion reactions. *Chemical Society Reviews*, *44*(8), 2060–2086. https://doi.org/10.1039/c4cs00470a

Joo, J., Kim, T., Lee, J., Choi, S. Il, & Lee, K. (2019). Morphology-Controlled Metal Sulfides and Phosphides for Electrochemical Water Splitting. *Advanced Materials*, *31*(14), 1806682. https://doi.org/10.1002/adma.201806682

Kaur, M., & Pal, K. (2019). Review on hydrogen storage materials and methods from an electrochemical viewpoint. *Journal of Energy Storage*, *23*(March), 234–249. https://doi.org/10.1016/j.est.2019.03.020

Kupka, J., & Budniok, A. (1990). Electrolytic oxygen evolution on Ni-Co-P alloys. *Journal of Applied Electrochemistry*, *20*(6), 1015–1020. https://doi.org/10.1007/BF01019582

Laursen, A. B., Patraju, K. R., Whitaker, M. J., Retuerto, M., Sarkar, T., Yao, N., ... Dismukes, G. C. (2015). Nanocrystalline Ni5P4: a hydrogen evolution electrocatalyst of exceptional efficiency in both alkaline and acidic media. *Energy Environ. Sci.*, *8*(3), 1027–1034. https://doi.org/10.1039/C4EE02940B

LeRoy, R. L. (1983). Industrial water splitting : Present and future. *International Journal of Hydrogen Energy*, *8*(6), 401–417. https://doi.org/https://doi.org/10.1016/0360-3199(83)90162-3

Lewis, N. S., & Nocera, D. G. (2006). Powering the planet: Chemical challenges in solar energy utilization. *Proceedings of the National Academy of Sciences*, *103*(43), 15729 LP – 15735. https://doi.org/10.1073/pnas.0603395103

Liang, H., Gandi, A. N., Anjum, D. H., Wang, X., Schwingenschlögl, U., & Alshareef, H. N. (2016). Plasma-Assisted Synthesis of NiCoP for Efficient Overall Water Splitting. *Nano Letters*, *16*(12), 7718–7725. https://doi.org/10.1021/acs.nanolett.6b03803

Liu, P., & Rodriguez, J. A. (2005). Catalysts for Hydrogen Evolution from the [NiFe] Hydrogenase to the Ni2P(001) Surface: The Importance of Ensemble Effect. *Journal of the American Chemical Society*,

127(42), 14871–14878. https://doi.org/10.1021/ja0540019

Liyanage, D. R., Danforth, S. J., Liu, Y., Bussell, M. E., & Brock, S. L. (2015). Simultaneous Control of Composition, Size, and Morphology in Discrete Ni2–xCoxP Nanoparticles. *Chemistry of Materials*, *27*(12), 4349–4357. https://doi.org/10.1021/acs.chemmater.5b00958

McEnaney, J. M., Chance Crompton, J., Callejas, J. F., Popczun, E. J., Read, C. G., Lewis, N. S., & Schaak, R. E. (2014). Electrocatalytic hydrogen evolution using amorphous tungsten phosphide nanoparticles. *Chem. Commun.*, *50*(75), 11026–11028. https://doi.org/10.1039/C4CC04709E

Mignon, I., & Bergek, A. (2016). System- and actor-level challenges for diffusion of renewable electricity technologies : an international comparison. *Journal of Cleaner Production*, *128*, 105–115. https://doi.org/10.1016/j.jclepro.2015.09.048

Morales-Guio, C. G., Stern, L. A., & Hu, X. (2014). Nanostructured hydrotreating catalysts for electrochemical hydrogen evolution. *Chemical Society Reviews*, *43*(18), 6555–6569. https://doi.org/10.1039/c3cs60468c

Nikolaidis, P., & Poullikkas, A. (2017). A comparative overview of hydrogen production processes. *Renewable and Sustainable Energy Reviews*, *67*, 597–611. https://doi.org/10.1016/j.rser.2016.09.044

Oyama, S. T., Gott, T., Zhao, H., & Lee, Y.-K. (2009). Transition metal phosphide hydroprocessing catalysts: A review. *Catalysis Today*, *143*(1), 94–107. https://doi.org/https://doi.org/10.1016/j.cattod.2008.09.019

Pan, Y., Liu, Y., Zhao, J., Yang, K., Liang, J., Liu, D., … Liu, C. (2015). Monodispersed nickel phosphide nanocrystals with different phases: synthesis{,} characterization and electrocatalytic properties for hydrogen evolution. *J. Mater. Chem. A*, *3*(4), 1656–1665. https://doi.org/10.1039/C4TA04867A

Pi, Y., Zhang, N., Guo, S., Guo, J., & Huang, X. (2016). Ultrathin Laminar Ir Superstructure as Highly Efficient Oxygen Evolution Electrocatalyst in Broad pH Range. *Nano Letters*, *16*(7), 4424–4430. https://doi.org/10.1021/acs.nanolett.6b01554

Pinto, F., Varela, F. T., Gonçalves, M., Neto André, R., Costa, P., & Mendes, B. (2014). Production of bio-hydrocarbons by hydrotreating of pomace oil. *Fuel*, *116*, 84–93. https://doi.org/10.1016/j.fuel.2013.07.116

Popczun, E. J., Read, C. G., Roske, C. W., Lewis, N. S., & Schaak, R. E. (2014). Highly Active Electrocatalysis of the Hydrogen Evolution Reaction by Cobalt Phosphide Nanoparticles. *Angewandte Chemie International Edition*, *53*(21), 5427–5430. https://doi.org/10.1002/anie.201402646

Reichelt, R. (2007). Scanning Electron Microscopy. In P. W. Hawkes & J. C. H. Spence (Eds.), *Science of Microscopy* (pp. 133–272). New York, NY: Springer New York. https://doi.org/10.1007/978-0-387-49762-4_3

Ryu, J., Jung, N., Jang, J. H., Kim, H.-J., & Yoo, S. J. (2015). In Situ Transformation of Hydrogen-Evolving CoP Nanoparticles: Toward Efficient Oxygen Evolution Catalysts Bearing Dispersed Morphologies with Co-oxo/hydroxo Molecular Units. *ACS Catalysis*, *5*(7), 4066–4074. https://doi.org/10.1021/acscatal.5b00349

Schipper, D. E., Zhao, Z., Thirumalai, H., Leitner, A. P., Donaldson, S. L., Kumar, A., ... Whitmire, K. H. (2018). Effects of Catalyst Phase on the Hydrogen Evolution Reaction of Water Splitting: Preparation of Phase-Pure Films of FeP, Fe2P, and Fe3P and Their Relative Catalytic Activities. *Chemistry of Materials*, *30*(10), 3588–3598. https://doi.org/10.1021/acs.chemmater.8b01624

She, Z. W., Kibsgaard, J., Dickens, C. F., Chorkendorff, I., Nørskov, J. K., & Jaramillo, T. F. (2017). Combining theory and experiment in electrocatalysis: Insights into materials design. *Science*, *355*(6321), 4998. https://doi.org/10.1126/science.aad4998

Shi, Y., & Zhang, B. (2016). Recent advances in transition metal phosphide nanomaterials: synthesis and applications in hydrogen evolution reaction. *Chemical Society Reviews*, *45*(6), 1529–1541. https://doi.org/10.1039/C5CS00434A

Staffell, I., Scamman, D., Velazquez Abad, A., Balcombe, P., Dodds, P. E., Ekins, P., ... Ward, K. R. (2019). The role of hydrogen and fuel cells in the global energy system. *Energy and Environmental Science*, *12*(2), 463–491. https://doi.org/10.1039/c8ee01157e

Stern, L.-A., Feng, L., Song, F., & Hu, X. (2015). Ni2P as a Janus catalyst for water splitting: the oxygen evolution activity of Ni2P nanoparticles. *Energy Environ. Sci.*, *8*(8), 2347–2351. https://doi.org/10.1039/C5EE01155H

Suen, N. T., Hung, S. F., Quan, Q., Zhang, N., Xu, Y. J., & Chen, H. M. (2017). Electrocatalysis for the oxygen evolution reaction: Recent development and future perspectives. *Chemical Society Reviews*, *46*(2), 337–365. https://doi.org/10.1039/c6cs00328a

Taljan, G., & Gubina, A. F. (2009). Energy-based system well-being analysis for small systems with intermittent renewable energy sources. *Renewable Energy*, *34*(12), 2651–2661. https://doi.org/10.1016/j.renene.2009.05.012

Tian, J., Liu, Q., Asiri, A. M., & Sun, X. (2014). Self-Supported Nanoporous Cobalt Phosphide Nanowire Arrays:

An Efficient 3D Hydrogen-Evolving Cathode over the Wide Range of pH 0–14. *Journal of the American Chemical Society*, *136*(21), 7587–7590. https://doi.org/10.1021/ja503372r

Verma, H. R. (2007). X-Ray Photoelectron Spectroscopy. In *Atomic and Nuclear Analytical Methods* (pp. 213–241). Berlin Heidelberg: Springer Berlin Heidelberg. https://doi.org/https://doi.org/10.1007/978-3-540-30279-7_5

Walter, M. G., Warren, E. L., McKone, J. R., Boettcher, S. W., Mi, Q., Santori, E. A., & Lewis, N. S. (2010). Solar water splitting cells. *Chemical Reviews*, *110*(11), 6446–6473. https://doi.org/10.1021/cr1002326

Wang, P., Song, F., Amal, R., Ng, Y. H., & Hu, X. (2016). Efficient Water Splitting Catalyzed by Cobalt Phosphide-Based Nanoneedle Arrays Supported on Carbon Cloth. *ChemSusChem*, *9*(5), 472–477. https://doi.org/10.1002/cssc.201501599

Wang, X., Kolen'ko, Y. V, Bao, X.-Q., Kovnir, K., & Liu, L. (2015). One-Step Synthesis of Self-Supported Nickel Phosphide Nanosheet Array Cathodes for Efficient Electrocatalytic Hydrogen Generation. *Angewandte Chemie International Edition*, *54*(28), 8188–8192. https://doi.org/10.1002/anie.201502577

Wang, Y., Kong, B., Zhao, D., Wang, H., & Selomulya, C. (2017). Strategies for developing transition metal phosphides as heterogeneous electrocatalysts for water splitting. *Nano Today*, *15*, 26–55. https://doi.org/10.1016/j.nantod.2017.06.006

Wikipedia contributors. (2011, July 31). X-ray photoelectron spectroscopy. In *Wikipedia, The Free Encyclopedia*. Retrieved October 7, 2019, from https://en.wikipedia.org/w/index.php?title=X-ray_photoelectron_spectroscopy&oldid=908738578

Williams, D. B., & Carter, C. B. (1996). The Transmission Electron Microscope. In D. B. Williams & C. B. Carter (Eds.), *Transmission Electron Microscopy* (pp. 3–17). Boston, MA: Springer US. https://doi.org/10.1007/978-1-4757-2519-3_1

Wu, T., Pi, M., Zhang, D., & Chen, S. (2016). 3D structured porous CoP3 nanoneedle arrays as an efficient bifunctional electrocatalyst for the evolution reaction of hydrogen and oxygen. *J. Mater. Chem. A*, *4*(38), 14539–14544. https://doi.org/10.1039/C6TA05838H

Xiao, P., Sk, M. A., Thia, L., Ge, X., Lim, R. J., Wang, J.-Y., … Wang, X. (2014). Molybdenum phosphide as an efficient electrocatalyst for the hydrogen evolution reaction. *Energy Environ. Sci.*, *7*(8), 2624–2629. https://doi.org/10.1039/C4EE00957F

Xiong, B., Chen, L., & Shi, J. (2018). Anion-Containing Noble-Metal-Free Bifunctional Electrocatalysts for

Overall Water Splitting. *ACS Catalysis*, *8*(4), 3688–3707. https://doi.org/10.1021/acscatal.7b04286

Xu, J., Li, J., Xiong, D., Zhang, B., Liu, Y., Wu, K.-H., … Liu, L. (2018). Trends in activity for the oxygen evolution reaction on transition metal (M = Fe, Co, Ni) phosphide pre-catalysts. *Chemical Science*, *9*(14), 3470–3476. https://doi.org/10.1039/C7SC05033J

Xu, J., Liu, Y., Li, J., Amorim, I., Zhang, B., Xiong, D., … Liu, L. (2018). Hollow cobalt phosphide octahedral pre-catalysts with exceptionally high intrinsic catalytic activity for electro-oxidation of water and methanol. *Journal of Materials Chemistry A*, *6*(42), 20646–20652. https://doi.org/10.1039/C8TA07958G

Xu, J., Xiong, D., Amorim, I., & Liu, L. (2018). Template-Free Synthesis of Hollow Iron Phosphide–Phosphate Composite Nanotubes for Use as Active and Stable Oxygen Evolution Electrocatalysts. *ACS Applied Nano Materials*, *1*(2), 617–624. https://doi.org/10.1021/acsanm.7b00122

Yan, Y., He, T., Zhao, B., Qi, K., Liu, H., & Xia, B. Y. (2018). Metal/covalent–organic frameworks-based electrocatalysts for water splitting. *Journal of Materials Chemistry A*, *6*(33), 15905–15926. https://doi.org/10.1039/C8TA05985C

You, B., & Sun, Y. (2018). Innovative Strategies for Electrocatalytic Water Splitting. *Accounts of Chemical Research*, *51*(7), 1571–1580. https://doi.org/10.1021/acs.accounts.8b00002

Yu, J., Li, Q., Li, Y., Xu, C.-Y., Zhen, L., Dravid, V. P., & Wu, J. (2016). Ternary Metal Phosphide with Triple-Layered Structure as a Low-Cost and Efficient Electrocatalyst for Bifunctional Water Splitting. *Advanced Functional Materials*, *26*(42), 7644–7651. https://doi.org/10.1002/adfm.201603727

Yu, X., Feng, Y., Jeon, Y., Guan, B., Lou, X. W., & Paik, U. (2016). Formation of Ni–Co–MoS2 Nanoboxes with Enhanced Electrocatalytic Activity for Hydrogen Evolution. *Advanced Materials*, *28*(40), 9006–9011. https://doi.org/10.1002/adma.201601188

Zeng, K., & Zhang, D. (2010). Recent progress in alkaline water splitting for hydrogen production and applications. *Progress in Energy and Combustion Science*, *36*(3), 307–326. https://doi.org/10.1016/j.pecs.2009.11.002

Zhang, C., Huang, Y., Yu, Y., Zhang, J., Zhuo, S., & Zhang, B. (2017). Sub-1.1 nm ultrathin porous CoP nanosheets with dominant reactive {200} facets: a high mass activity and efficient electrocatalyst for the hydrogen evolution reaction. *Chem. Sci.*, *8*(4), 2769–2775. https://doi.org/10.1039/C6SC05687C

Zhang, Y., Xiao, J., Lv, Q., & Wang, S. (2018). Self-supported transition metal phosphide based electrodes as high-efficient water splitting cathodes. *Frontiers of Chemical Science and Engineering*, *12*(3), 494–508. https://doi.org/10.1007/s11705-018-1732-9

Zhao, G., Rui, K., Dou, S. X., & Sun, W. (2018). Heterostructures for Electrochemical Hydrogen Evolution Reaction: A Review. *Advanced Functional Materials*, *28*(43), 1803291. https://doi.org/10.1002/adfm.201803291

Zhu, Y.-P., Liu, Y.-P., Ren, T.-Z., & Yuan, Z.-Y. (2015). Self-Supported Cobalt Phosphide Mesoporous Nanorod Arrays: A Flexible and Bifunctional Electrode for Highly Active Electrocatalytic Water Reduction and Oxidation. *Advanced Functional Materials*, *25*(47), 7337–7347. https://doi.org/10.1002/adfm.201503666